Actin Mediates the Nanoscale Membrane Organization of the Clustered Membrane Protein Influenza Hemagglutinin

Manasa V. Gudheti,[†△] Nikki M. Curthoys,[†△] Travis J. Gould,[†] Dahan Kim,[†] Mudalige S. Gunewardene,[†]
Kristin A. Gabor,[†‡§] Julie A. Gosse,[‡§] Carol H. Kim,[‡§] Joshua Zimmerberg,[¶] and Samuel T. Hess[†§]*
[†]Department of Physics and Astronomy, [‡]Department of Molecular and Biomedical Sciences, and [§]Graduate School of Biomedical Science and Engineering, University of Maine, Orono, Maine; and [¶]Program in Physical Biology, Eunice Kennedy Shriver National Institute of Child Health and Human Development, National Institutes of Health, Bethesda, Maryland

ABSTRACT The influenza viral membrane protein hemagglutinin (HA) is required at high concentrations on virion and host-cell membranes for infectivity. Because the role of actin in membrane organization is not completely understood, we quantified the relationship between HA and host-cell actin at the nanoscale. Results obtained using superresolution fluorescence photoactivation localization microscopy (FPALM) in nonpolarized cells show that HA clusters colocalize with actin-rich membrane regions (ARMRs). Individual molecular trajectories in live cells indicate restricted HA mobility in ARMRs, and actin disruption caused specific changes to HA clustering. Surprisingly, the actin-binding protein cofilin was excluded from some regions within several hundred nanometers of HA clusters, suggesting that HA clusters or adjacent proteins within the same clusters influence local actin structure. Thus, with the use of imaging, we demonstrate a dynamic relationship between glycoprotein membrane organization and the actin cytoskeleton at the nanoscale.

INTRODUCTION

Cell plasma membranes are widely understood to be laterally heterogeneous, and membrane-associated proteins can be distributed in complexes and aggregations that span a range of length scales (1,2). In one cell, a single species of protein can have one subset undergoing Brownian diffusion whereas other subsets undergo confined or anomalous diffusion (3). Indeed, early evidence from various methods suggested that the lateral mobility of proteins in cell membranes could be restrained by forces beyond those of the viscosity of the membrane itself, such as those exerted by the actin cytoskeleton (4,5), and such restraints may help to form or maintain protein clusters by corralling the proteins together between barriers.

The idea that the cytoskeleton can organize protein clusters or membrane domains by acting as a physical structure that confines the diffusion of membrane-bound proteins and lipids is long-standing (6,7), and many studies have emphasized the importance of the cytoskeleton in membrane organization (8–12). Investigators have proposed different mechanisms for the role of actin. Transmembrane (TM) proteins bound to the underlying actin cytoskeleton may act as obstacles that restrict the lateral diffusion of other proteins in the bilayer (6), clustering of membrane proteins may be promoted by local enrichment of cortical actin filaments (13), or the actin filaments themselves may act as barriers to lateral diffusion (14). Additionally, the actin cytoskeleton can interact with the plasma membrane through actin-binding proteins (ABPs) such as spectrin, filamin, and ezrin, and such interactions have also been hypothesized to aid in the organization of membrane proteins (15,16). Discriminating among the diverse range of models that have been proposed to explain how actin can alter the diffusion and cell-surface distribution of membrane-bound proteins has proved to be challenging. Although we have gained a considerable understanding of membrane organization with the use of techniques such as Förster resonance energy transfer (FRET (8)), single-particle tracking (SPT (17)), and fluorescence recovery after photobleaching (FRAP (18)), the submicron length scale and dynamic nature of whole native membrane domains in living cells make these domains unsuitable for imaging by either conventional light microscopy or electron microscopy. This technical impasse has resulted in a strong need for information about the size range, composition, and dynamic properties of protein clusters in unperturbed cells. Moreover, the precise spatial and dynamic relationships between actin and membrane proteins at relevant scales have remained elusive.

To investigate membrane organization and its role in viral infection, we studied hemagglutinin (HA), the TM viral fusion protein from influenza (19), expressed in NIH3T3-HAb2 fibroblast cells. The local concentration of HA on the surface of virions is crucial for influenza entry via membrane fusion (20), and HA concentration on host-cell membranes is crucial for release of bud particles from infected cells (21). Both of these processes are promoted by

---

Submitted June 8, 2012, and accepted for publication March 20, 2013.

[△]Manasa V. Gudheti and Nikki M. Curthoys contributed equally to this work.

*Correspondence: sam.hess@umit.maine.edu

Manasa V. Gudheti's present address is Department of Biology, University of Utah, and Vutara, Inc., Salt Lake City, Utah.

Travis J. Gould's present address is Department of Cell Biology, Yale University School of Medicine, New Haven, Connecticut.

Editor: Lukas Tamm.

0006-3495/13/05/2182/11 $2.00

http://dx.doi.org/10.1016/j.bpj.2013.03.054

clustering of HA at the host-cell membrane and depend on membrane organization at the nanoscale (22). Intriguingly, influenza viruses analyzed by mass spectrometry were found to contain β-actin and a number of actin-associated proteins, including cofilin, several annexins, tropomyosins, and profilin (23). Although colocalization between HA and actin on coarse spatial scales has been observed (24), direct binding between HA and actin or ABPs (in the absence of other viral components) has not yet been reported. Rather, HA may influence actin organization through signaling pathways. For example, the host-cell surface accumulation of HA and its clustering is required for influenza infection because membrane accumulation of HA triggers activation of the Raf/ERK/MEK cascade via protein kinase C α (PKCα) activation and induces export of the viral ribonucleoprotein from the host-cell nucleus (25).

Our goal in this work was to elucidate the role of the actin cytoskeleton in cell membrane organization, using HA as a canonical membrane-associated protein that is known to organize into nanoscopic and larger scale domains (26,27). In particular, we focused on the question of how actin mediates HA dynamics and clustering at the nanoscale, using the superresolution method fluorescence photoactivation localization microscopy (FPALM) (28). Our results reveal how actin distribution and the perturbation of the actin cytoskeletal network affect the membrane organization of this critical viral component—information that can be used to develop new antiviral therapies. Surprisingly, the ABP cofilin was excluded from regions within several hundred nanometers of HA clusters, suggesting that HA or adjacent proteins in the same clusters influence local actin structure. We propose a feedback mechanism that couples the clustering of HA at the cell surface to the distribution of ABPs adjacent to those clusters. This concept can serve as a general model for cross talk between membrane-associated proteins and the underlying cortical actin cytoskeleton.

MATERIALS AND METHODS

For more details regarding the materials and methods used in this work, see the Supporting Material.

Constructs

pDendra2-HA (29) and pPAmCherry-β-actin (30) (hereafter referred to as Dendra2-HA and PAmCherry-actin, respectively) were based on the pEGFP-N1 vector (Clontech, Mountain View, CA) and are described in detail elsewhere. The coding DNA of the hemagglutinin gene of the A/X-31B (Puerto Rico/8/1934-Aichi/2/1968) (H3N2)strain of influenza virus was used in the pDendra2-HA plasmid. pPAmCherry-cofilin (hereafter referred to as PAmCherry-cofilin) was made by cloning human (non-muscle) cofilin 1 (NCBI accession number: NM_005507.2) between BamHI-AgeI sites of the pEGFP-pPAmCherry vector. This vector is the same as that used for pPAmCherry-β-actin, with pEGFP replaced by pPAmCherry in pEGFP-N1 (Clontech).

Cell culture

NIH3T3-HAb2 fibroblast cells (NIH3T3 cells that stably overexpress the hemagglutinin gene of the A/Japan/305/57 H2N2 strain of human influenza virus (20,31)) were maintained in growth media (Dulbecco's modified Eagle's medium) supplemented with 10% calf bovine serum (ATCC, Manassas, VA) and antibiotics (100 U/mL penicillin and 100 μg/mL streptomycin; Gibco/Invitrogen, Carlsbad, CA), and cultured at 37°C in 5% CO_2.

Superresolution imaging

Cells were transfected using Lipofectamine 2000 (Life Technologies, Invitrogen) and constructs for fluorescent protein-tagged proteins of interest, plated in eight-well coverglass chambers (Nalge Nunc), and imaged according to established procedures (32). Imaged molecules were localized according to established procedures, and the determined coordinates for molecules that met thresholds for quality of fit and localization precision were further analyzed for clustering.

Nearest-neighbor-based cluster analysis

After identification and position averaging of molecules visible for more than one consecutive frame, fixed-cell data sets on HA comprised 23,120,711 localized molecules in NIH3T3-HAb2 cells. Clusters were identified by single-linkage cluster analysis (SLCA) (33). All molecules within a given distance d_c of one another were assigned to the same cluster. Using $d_c = 30$ nm, roughly equal to the position uncertainty for the majority of molecules, individual clusters could be identified from a set of coordinates. Similar results were obtained using $d_c = 40$ nm.

Cluster morphological properties

Given the coordinates of molecules determined to lie within the same cluster, the area and density (number of particles per unit area) were then determined for each cluster. The area was measured from the shape formed by stamping a circle of radius d_c around each molecule in the cluster and taking the area of that continuous shape. The density was calculated as the number of molecules per square micron of area in the cluster.

Actin cytoskeleton disruption and staining

NIH3T3-HAb2 cells were incubated with full growth media supplemented with 1 μM Latrunculin A (LatA) for 10 min, 1 μM Cytochalasin D (CytoD) for 60 min, 1 μM jasplakinolide (Jas) for 30 min, or 0.01% dimethyl sulfoxide (DMSO; control) for 60 min. Subsequently, the cells were rinsed three times with UV-bleached phosphate-buffered saline (PBS) and fixed in 4% paraformaldehyde in PBS at room temperature (RT) for 20 min before being rinsed a further three times and imaged in UV-bleached PBS. To visualize F-actin, Alexa 488 phalloidin (Life Technologies, Invitrogen) diluted 1:200 in PBS with 0.5% bovine serum albumin was added to the cells for 20 min at RT.

Confocal microscopy

An Olympus Fluoview FV1000 microscope was used to image Alexa 488 phalloidin at RT in the confocal mode. Images were obtained using either a 60×/1.2 NA water or a 60×/1.42 NA oil immersion objective with 488 nm excitation and 505–525 nm detection.

SLCA

Molecular positions were analyzed to determine clustering. As described previously (33,34), the positions of molecules that were within a maximum distance of 30 nm were defined as being within the same cluster. Using an iterative approach, we first identified all molecules within 30 nm of a given molecule and then added those to a list, searched all new molecules added to the list for neighbors within 30 nm, and repeated the process until all members of that cluster had been obtained. For more details, please see the Supporting Material.

RESULTS

HA colocalizes with actin at the nanoscale in both fixed and live cells at 37°C

For colocalization studies, we used Dendra2-HA and PAmCherry-actin plasmids transiently transfected into nonpolarized NIH3T3-HAb2 mouse fibroblast cells (20). We previously showed that PAmCherry-actin labels the same filamentous actin structures as phalloidin in NIH3T3-HAb2 cells (32). In this study, two-color FPALM revealed irregular clusters of HA and actin distributions in both fixed and live NIH3T3-HAb2 cells (Fig. 1) within ± 0.5 μm (the effective focal depth of this FPALM imaging) of bottom plasma membranes. Although Fig. 1 shows a striking example of elongated HA clusters, we observed considerable variability in cluster morphology from cell to cell and within cells, with most cells showing both elongated and more compact (i.e., globular) HA clusters, consistent with previously published work (26,27). Clusters of HA were often spatially colocalized with clusters of actin. Pair correlation analysis with bleed-through correction revealed a strong correlation between HA and actin in live NIH3T3-HAb2 cells (Fig. 1 *G*; $n = 10$ cells) on length scales of ~50 nm to >1 μm. The accumulation of actin and HA together at the bottom membrane raises the possibility that the clustering observed here represents projections of unclustered proteins distributed in convoluted membranes. However, evidence provided by electron microscopy imaging of NIH3T3-HAb2 membranes (27) indicates that the degree of membrane convolution in these cells is not sufficient to result in the clustering on the scales of hundreds of nanometers to micrometers we observed here with FPALM. We next imaged HA membrane domains and actin in fixed and live cells, and examined the timescale of their persistence in live cells. Through FPALM time-lapse imaging (Fig. 2, *B* and *C*), we were able to observe the persistence of HA clusters in living NIH3T3-HAb2 cells over many tens of seconds. To test whether the actin cytoskeleton was influencing local HA mobility, we measured the trajectories of individual HA molecules and compared them in regions of different actin densities.

HA mobility is dependent on local actin density

We obtained trajectories of individual HA molecules with a time resolution of 16.7 ms by localizing individual Dendra2-HA molecules as a function of time for several frames (ranging from two to 23 steps spanning tens to hundreds of milliseconds). We then analyzed these trajectories by diffusion analysis (see Eqs. 1 and 2 in the Supporting Material) to determine the mean-squared displacement (MSD) per unit time. For Dendra2-HA expressed alone and imaged in NIH3T3-HAb2 cells ($n = 29$ cells), the histogram of turn angles (defined as the angle between a given step of an individual molecule and the previous step) shows biases for angles 0° ± 45° (i.e., the molecule continues ahead, 25.15% ± 0.07% of all steps) and 180° ± 45° (i.e., the molecule reverses direction, 29.72% ± 0.07%), compared with 90° ± 45° (i.e., right turn, 22.55% ± 0.06%) and −90° ± 45° (left turn, 22.58% ± 0.06%; see Fig. S1).

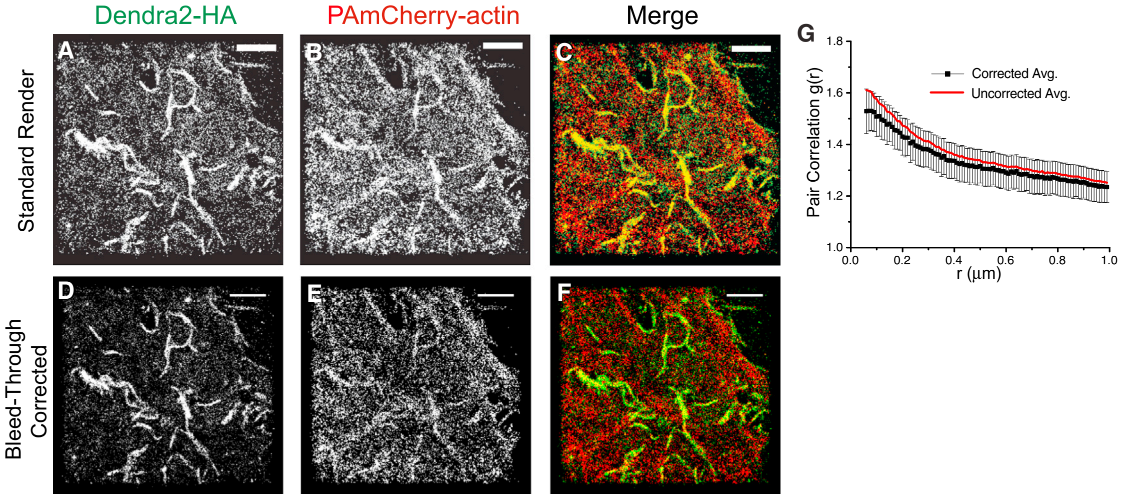

FIGURE 1 Two-color, live-cell FPALM imaging reveals a correlation between HA and actin in nonpolarized NIH3T3-HAb2 cells. (*A–C*) Clusters of Dendra2-HA (*A*, *green channel*) colocalize with PAmCherry-actin (*B*, *red channel*), shown merged in *C*. (*D–F*) Bleed-through corrected versions of panels *A–C*. (*G*) The pair correlation g(r) between HA and actin is significant (amplitude of one is random) with (*black points*) or without (*red points*) bleed-through correction. Data shown are the average of $n = 10$ live cells, mean ± SE. Scale bar = 2 μm.

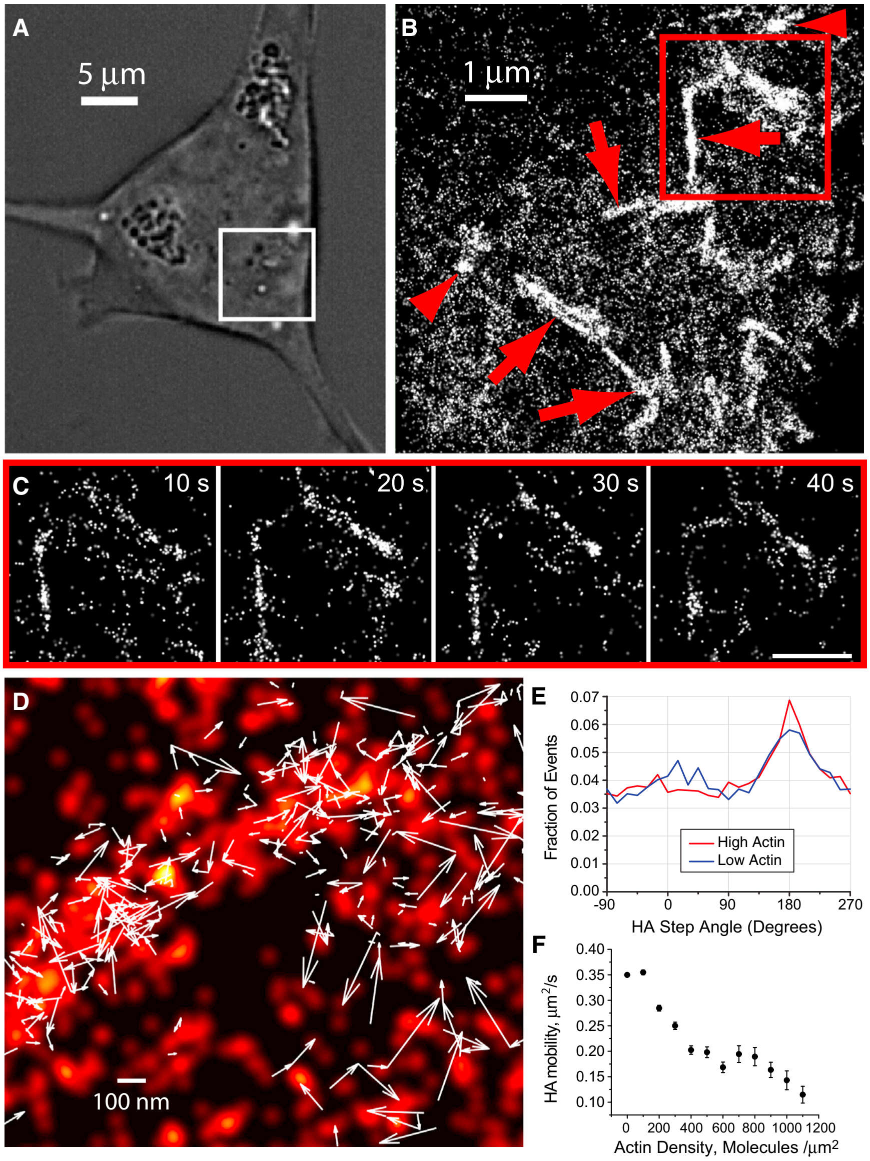

FIGURE 2 HA mobility differs according to the surrounding actin density. (*A*) Transmitted light image of a living NIH3T3-HAb2 cell. The area enclosed by the white box shows the region imaged in *B* obtained using FPALM. (*B*) Time-integrated (~217 s) FPALM image of Dendra2-HA (43,180 molecules) shows both linear (*red arrows*) and globular (*red arrowheads*) HA clusters. (*C*) Consecutive FPALM renderings in ~10 s intervals of the boxed region in *B* show persistent linear clusters as a function of time. Scale bar = 1 μm. (*D–F*) The dynamics of Dendra2-HA correlates with actin density. (*D*) Superimposed two-color (Dendra2-HA and PAmCherry-actin) live-cell FPALM image of PAmCherry-actin (*red pseudocolor*) and 377 trajectories of Dendra2-HA molecules (*white arrows*) in a living NIH3T3-HAb2 fibroblast at 37°C. (*E*) Histogram of HA turn angles (the angle of a given step measured relative to the previous step) for 26,669 molecules (trajectories) in $n = 19$ untreated cells in regions with below-median local actin density (*blue line*) and above-median actin density (*red line*). Trajectories were acquired at 31.75 ms/frame and lasted up to ~20 frames. (*F*) HA mobility (as measured by MSD per second) decreases with increasing actin density, suggesting that HA motion is restricted by actin-associated structures.

Next, we compared the trajectories of HA molecules in regions of above- and below-median actin density (see Supporting Material for definitions of each) in NIH3T3-HAb2 cells expressing both Dendra2-HA and PAmCherry-actin. HA molecules in regions of above-median actin density (Fig. 2 *E*, *red line*) were significantly less likely to take two consecutive steps in a given direction (within ±37.5° of the original direction; 22.2% ± 0.7% of events) than HA molecules in regions of below-median actin density (24.0% ± 0.7% of events; Fig. 2 *E*, *blue line*). Thus, the restriction of HA mobility was correlated with actin density. Furthermore, we measured the MSDs of individual HA molecules and found that, over tens of milliseconds, the step sizes of HA molecules reduced as local actin density increased (Fig. 2 *F*). We hypothesized that these trends reflected multiple populations of HA, with the confinement of each depending on the surrounding actin density. We therefore quantified the diffusion behavior of labeled HA molecules in live cells.

Two distinct populations of HA revealed by particle image correlation spectroscopy

In live NIH3T3-HAb2 cells, particle image correlation spectroscopy (PICS) analysis (35) of individual Dendra2-HA molecules (Fig. 3) revealed two populations of Dendra2-HA with distinct modes of diffusion. One population undergoes free diffusion (Fig. 3 *C*) with $D = 0.109 \pm 0.066$ μm^2/s (74% ± 7% of molecules) and the other (26% ± 7% of molecules) shows confined diffusion (Fig. 3 *D*) with $D = 0.028 \pm 0.018$ μm^2/s within a region of characteristic confinement size $L = 150 \pm 56$ nm (see

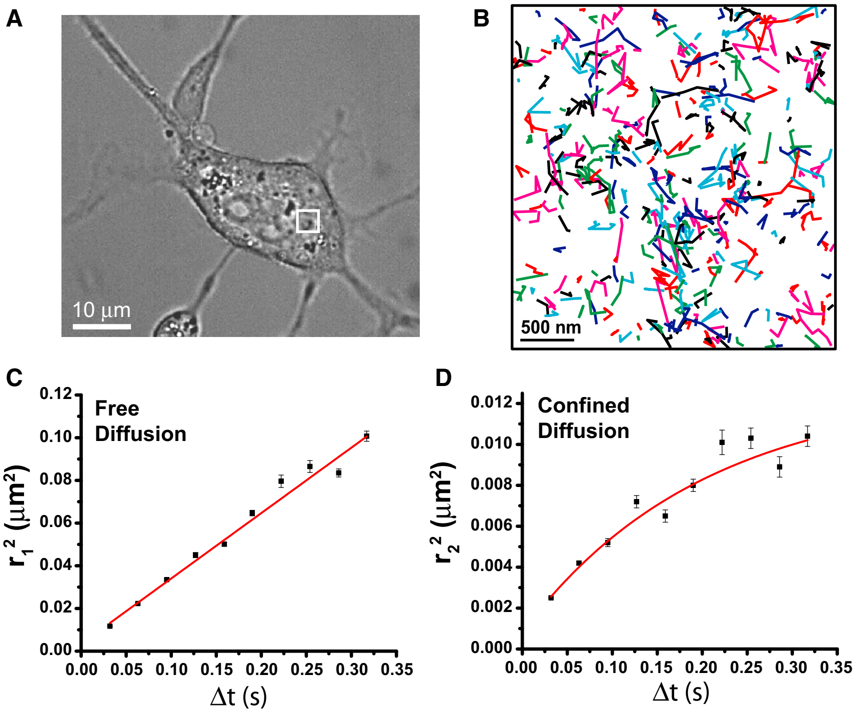

FIGURE 3 Analysis of trajectories of individual HA molecules by PICS within a living NIH3T3-HAb2 cell at 37°C shows two populations of HA molecules with distinct mobilities. (*A*) Transmitted light image of a living NIH3T3-HAb2 cell transfected with Dendra2-HA at 37°C. (*B*) The white box in *A* shows a region of the plasma membrane imaged by FPALM, in which the trajectories of individual molecules were determined over durations from 16.7 ms to 1.01 s (trajectories were between one and 32 steps at 16.7–31.7 ms per step). The time dependence of the displacements of the HA molecules was analyzed by PICS (35), revealing two distinct populations of HA molecules. (*C*) The first population (74% ± 7%) had a diffusion coefficient $D_1 = 0.109 \pm 0.066\ \mu m^2/s$ and underwent normal Brownian free diffusion within the uncertainties of the measurement. (*D*) In contrast, the second population (26% ± 7%) had a significantly lower diffusion coefficient $D_2 = 0.026 \pm 0.018\ \mu m^2/s$ and underwent confined diffusion within a region of size $L = 150 \pm 56$ nm. The relationship in *D* could not be fit with a straight line.

Eq. 5 in the Supporting Material for details of the analysis). Note that these results do not preclude the existence of more than two HA populations, but suggest that at least two must be invoked to describe the observed distribution of MSDs of HA as a function of time. The confined population suggests that lateral motion of HA molecules is restricted.

Actin regulates HA cluster morphology in nonpolarized NIH3T3-HAb2 fibroblast cells: native HA cluster morphology

We next examined the HA-actin relationship at the scale of a cluster, the biological membrane structure that precedes viral assembly and enables sufficient HA densities for infectivity (22). First, we analyzed the positions of 23,120,711 localized Dendra2-HA molecules in fixed NIH3T3-HAb2 cells (Fig. 4) using SLCA (33,36) to quantify the cluster area and density (Table S1). Clusters were defined by a maximum HA-HA radial separation of 30 nm for nearest neighbors within the same cluster. These analyses identified 22,186 clusters of at least 50 localized HA molecules, and 6793 clusters with at least 200 HA molecules ($n = 25$ cells). Area and density histograms for all HA clusters (not just those with at least 50 molecules) are shown in Figs. S2 and S3. These histograms demonstrate a range of cluster areas from just a few molecules up to nearly 0.2 μm^2 and a range of densities from ~500 HA/μm^2 up to nearly 10,000 HA/μm^2. As expected from the live-cell data on HA dynamics, elongated and branched clusters of HA were observed in control NIH3T3-HAb2 cells (Figs. 2, *A–C*, and 4 *A*) that sometimes showed distinct angular junctions suggestive of a network of linear structures.

Actin cytoskeletal disrupters cause specific changes to HA cluster density and area

If actin mediates HA clustering, then disruption of actin should alter HA clustering. Because HA mobility was found to be restricted within actin-rich membrane regions (ARMRs), we hypothesized that reducing or increasing the density of actin filaments would alter HA clustering. LatA sequesters actin monomers, thereby inhibiting actin polymerization (37). CytoD selectively binds filament barbed ends and blocks the addition of actin monomers (38). These agents can therefore reduce the total amount of filamentous cellular actin by interrupting actin treadmilling in mechanistically distinct ways. Conversely, Jas binds actin filaments and inhibits actin depolymerization (39), and thus can increase the fraction of filamentous cellular actin. Confocal images of Alexa-488-phalloidin-labeled NIH3T3-HAb2 cells (Fig. S4) treated with actin disrupters confirmed that stress fibers persisted with Jas treatment but were severely reduced in number with LatA or CytoD treatment, as expected. Confocal imaging of Dendra2-HA and Alexa-680-phalloidin confirmed the colocalization of HA with endogenous actin (Fig. S5). We characterized the effects of each of these actin-disrupting drugs on the morphology of HA clusters in Dendra2-HA-transfected NIH3T3-HAb2 cells (Fig. 4).

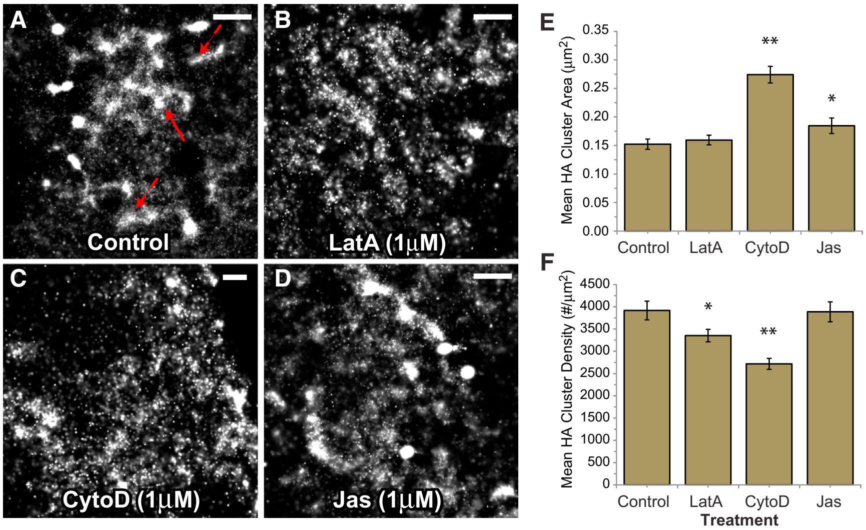

FIGURE 4 Actin mediates nanoscale HA cluster morphology. (*A*) Clusters of Dendra2-HA in fixed NIH3T3-HAb2 fibroblasts were imaged by FPALM after incubation with actin-disrupting drugs. HA clusters in control cells (imaged in 0.01% DMSO as vehicle control for actin-disrupting drugs) are either linear (*dashed arrows*) or globular (*solid arrows*). (*B–D*) A range of cluster morphologies is also observed in cells treated with actin disruptors: (*B*) 1μM Lat A for 10 min, (*C*) 1 μM CytoD for 60 min, and (*D*) 1 μM Jas for 30 min. The media for all treatments also contained 0.01% DMSO. Scale bar = 1 μm. (*E* and *F*) Treated cells show significant differences compared with controls in terms of (*E*) mean HA cluster area and (*F*) cluster density (i.e., number of HA molecules per cluster) measured for at least 149 clusters per treatment type. Statistical significance is indicated by a single asterisk (*$p < 0.05$) or double asterisk (**$p < 0.001$) as reported by Student's *t*-test comparing control with treatment means. Bars indicate means ± SE. For details on cluster comparisons, see Table S1.

Clusters were analyzed using SLCA (see Materials and Methods, and Supporting Material), which defines a cluster as any HA molecules within 30 nm of each other. SLCA (34,36) and pair correlation (32,40,41) are complementary methods for quantifying the properties of molecular clusters. The pair correlation provides a probability distribution (relative to random) of finding an HA molecule as a function of radial distance from another HA molecule. The density and size information extracted from pair correlation is an average over many molecules in many clusters. SLCA identifies individual clusters based on a maximum NN distance, and therefore can be used to measure the distribution of individual cluster properties (34). To quantify the role of actin on HA cluster area and density, we analyzed clusters of HA in cells treated with 1 μM LatA for 10 min, 1 μM CytoD for 60 min, or 1 μM Jas for 30 min, and compared them with HA clusters in corresponding vehicle (0.01% DMSO)-treated controls. The trends for clusters of $\geq$200 HA (see Table S1) and $\geq$50 HA molecules (not shown) were similar. Each actin-disrupting drug had specific effects on areas of HA clusters and the density of HA molecules within them (Fig. 4). LatA treatment resulted in a significant decrease in the mean density of HA within clusters, but no change in mean cluster area. CytoD induced a significant decrease in HA density within clusters and a significant increase in mean cluster area. Jas induced a significant increase in mean cluster area, but did not alter the mean density of HA within clusters (Fig. 4; Table S1).

Together, the results of these actin-disruption experiments indicate that actin can mediate the size and density of clusters of the membrane-associated protein HA. Because the ABP cofilin has been shown to be important in regulating actin structure across various cellular contexts (42–66), we next examined the relationship between HA clustering and cofilin distribution.

Cofilin is excluded from clusters of HA in NIH3T3-HAb2 cells

Two-color FPALM imaging of Dendra2-HA and PAmCherry-cofilin in transfected NIH3T3-HAb2 cells (Fig. 5) revealed that clusters of HA were predominantly surrounded by areas of cofilin exclusion, spanning hundreds of nanometers to micrometers. This exclusion was not absolute, however, and small, dense clusters of HA were sometimes colocalized with cofilin. Images were taken with an effective focal depth of 0.5 μm from the bottom membrane in fixed NIH3T3-HAb2 cells. Aside from areas within a lateral radius of 1–2 μm from HA clusters, cofilin was generally distributed diffusely throughout the cells. Quantification of the pair cross-correlation between HA and cofilin revealed, on the average ($n = 14$ cells), anticorrelation on length scales of ~150 nm to >1 μm (Fig. 5 *D*).

In summary, we show here that domains of the membrane-associated protein HA associate with specific local enrichments in actin, underlying actin can influence the organization of HA in these domains, and these domains predominantly exclude the ABP cofilin.

DISCUSSION

Imaging of HA clusters demonstrates mediation of membrane protein domains by the actin cytoskeleton on micro- and nanoscales

FPALM, which allows one to examine the dynamics of the molecular organization of cell membranes at the nanoscale, was used to image the relationship between actin and HA, a canonical example of a clustered membrane protein relevant to viral infection. Several surprising findings emerged. In the absence of any other viral components, HA was concentrated in ARMRs on nanometer length

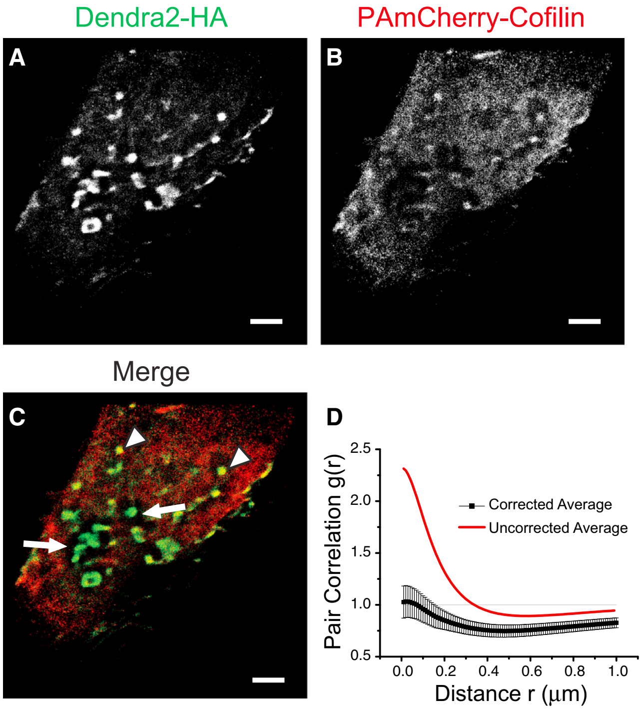

FIGURE 5 Cofilin is differentially excluded from HA clusters. Clusters of Dendra2-HA and PAmCherry-cofilin were imaged by two-color FPALM in fixed NIH3T3-HAb2 cells. (*A*, *green channel*) Clusters of HA span a range of length scales. (*B*, *red channel*) Cofilin was dispersed diffusely throughout the cell, except for areas surrounding HA clusters. (*C*) Merge. Extending hundreds of nanometers to micrometers from the periphery of HA clusters was typically a zone excluding cofilin (*white arrows*), although this pattern was not absolute. Some small HA clusters colocalized with cofilin clusters (*white arrowheads*). These images were taken at the bottom membrane with an effective focal depth of ±0.5 μm. Scale bar = 2 μm. (*D*) The pair-cross-correlation function for HA and cofilin depends strongly on bleed-through correction. The uncorrected curve (*red line*) overestimates correlation and underestimates anticorrelation. The corrected (*black points* ± SE, $n = 14$ fixed cells) shows significant anticorrelation, especially on length scales of ~600 nm.

scales in nonpolarized NIH3T3-HAb2 cells. In many cases, clustered structures hundreds of nanometers long, containing both HA and actin, were observed at physiological temperatures.

On the average, pair correlation analyses suggested an ~2-fold enrichment of HA in regions within 100 nm of actin-enriched regions. Based on the relatively large amplitude of the pair correlation (Fig. 1 *G*) from ~50 nm to >1 μm (compared with that expected for an uncorrelated distribution), HA and actin colocalize over a range of length scales. One caveat to this result is that all two-color FPALM distances are measured as a projection onto the x-y plane and do not account for any separation in the axial direction (z) other than the coarse discrimination in z due to the depth of field (±0.5 μm from the focal plane). However, based on electron microscopy of the same cell type by serial section (27), the z-position variation of the coverslip-proximal membrane does not explain the observed clustering.

The use of SLCA enabled us to measure the distribution of HA cluster areas and densities (the distribution contains far more information than the average cluster size). Such data are potentially useful for quantitatively testing physical membrane models of protein clustering, for example, or for determining the fraction of membrane clusters with a minimum area or density.

Disruption of actin caused HA clusters to change in size and density. The disruptive effect was specific to the agent being used: LatA significantly reduced the densities of HA within clusters (number of HA molecules/cluster unit area), and CytoD significantly increased the cluster area and also significantly reduced the HA density within clusters (Fig. 4, *A*–*C*, *E*, and *F*). Although CytoD does inhibit elongation at the barbed ends of actin filaments, it does not inhibit the de novo nucleation of actin filaments, and thus it could be expected to have a less stringent effect on actin filament load than LatA. We propose that the decreases in HA density within clusters seen with LatA and CytoD treatments could result from either the lateral dispersion of previously clustered HA molecules or the dispersal and reformation of less dense de novo clusters after drug treatments. We believe the former possibility applies to our models (Fig. S6), although the principles of underlying actin organization are the same for both scenarios. Because actin disruptors also cause changes in cell morphology, these changes may also contribute to the observed changes in cluster morphology.

If the actin filaments themselves serve as obstacles to cage each cluster, then depolymerizing these filaments should result in the dispersal of molecules in these clusters. Indeed, this is consistent with the results we observed after treatment with LatA or CytoD. In the context of such a confinement model, one would also expect that Jas treatment, by stabilizing the actin filament barriers, would keep the HA cluster sizes constant. However, Jas treatment resulted in increased HA cluster areas, indicating a mechanism whereby actin density is positively correlated with HA clustering, and increases in cortical actin filament density stabilize existing membrane domains and their peripheries (Fig. 4 *E*). Similarly, instead of finding that clusters had an anticorrelation or no association with actin, as might be expected if individual actin filaments were confining whole clusters, we observed the colocalization of actin and HA at length scales spanning from tens of nanometers up to several micrometers. The alteration in HA cluster density and size with these actin-disrupting agents instead indicates that individual actin filaments (at an increased density adjacent to the HA cluster) may provide points of anchor for clustered membrane proteins.

We observed a striking lateral heterogeneity in the density of actin, and differences in the movement characteristics of HA molecules in regions of high or low actin density. Other imaging studies have illustrated the three-dimensionality of the actin cytoskeleton (67,68), and we propose that areas of dense cortical actin meshwork provide one structural basis for cluster cohesion. The highly protein-specific segregation of membrane proteins (8) is not easily explained by models that invoke arrangements of TM proteins to reduce the lateral diffusion of membrane components (see Chichili and Rodgers (13) for review). Furthermore, we observed that actin and HA colocalize on the nanoscale, which suggests that actin and membrane proteins work in concert on molecular length scales to stabilize membrane domains.

On timescales of tens of milliseconds, the motion of HA molecules was slower in proximity to actin (Fig. 2 *F*). The peak at ~0° in the histogram of HA turn angles (Fig. 2 *E*) corresponds to HA molecules that took two successive steps in the same direction. The peak at ~180° corresponds to HA molecules that took one step in a given direction, followed by a step in the opposite direction. The strong biases (peaks) in the histogram as a function of angle suggest confinement of HA. The dependence of the frequency of these steps on actin density suggests a role for actin in the confinement. These findings suggest that ARMRs or other actin-associated cell components constrain the motion of HA. The colocalization of HA with actin and the elongated HA cluster shape further support this interpretation.

HA clusters are associated with heterogeneous cofilin distribution: cluster-actin feedback

Cofilin is an ABP that can act to increase the dissociation (off) rates of actin monomers from filaments (48), nucleate actin filaments (44), or sever actin filaments (69) depending on the cofilin/actin molar ratios. Cofilin is implicated in a range of diverse cellular processes, including regulation of actin dynamics during cell motility and leading-edge protrusion (43).

Our finding that the actin remodeling protein cofilin is laterally excluded from regions within several hundred nanometers of HA clusters suggests that HA can directly or indirectly mediate the spatial distribution of ABPs. HA mediation of the distribution of cofilin is expected to have an effect on actin organization that provides a (possible) mechanism for two-way coupling between clustering of membrane proteins and the local actin environment (Fig. 6).

Although there is considerable evidence for interactions between other influenza viral components and actin, we found no published evidence for HA interacting directly with actin. However, surface accumulation of HA can activate the PKCα and Raf/MEK/ERK signaling pathways (25), which both depend on and mediate actin structure (70,71). Thus, although we have not demonstrated the role of signaling in the observed HA and cofilin distributions, pathways have been identified through which HA could mediate actin and ABP organization.

Lateral mobility of HA: dynamic properties depend on local actin density

The dynamic nature of the actin cytoskeleton cannot be easily portrayed in a static figure. The observed effects of a 10 min LatA treatment on HA cluster morphology indicate that the actin filaments underlying these HA domains are likely turning over within this time. This highlights an important point: if membrane-associated actin filaments were dynamically treadmilling, one would expect attachments between HA and actin to be transitory, as has been proposed for potassium channels in living cell membranes (17).

We observed two mobile populations of HA: one fraction (74% ± 7%) with a diffusion coefficient ($D_1 = 0.109 \pm 0.066\ \mu m^2/s$) that is consistent with the mobile fraction and diffusion coefficient measured by FRAP at 37°C (18,72). Note that the interpretation of the fraction of the two HA populations could be complicated by exchange

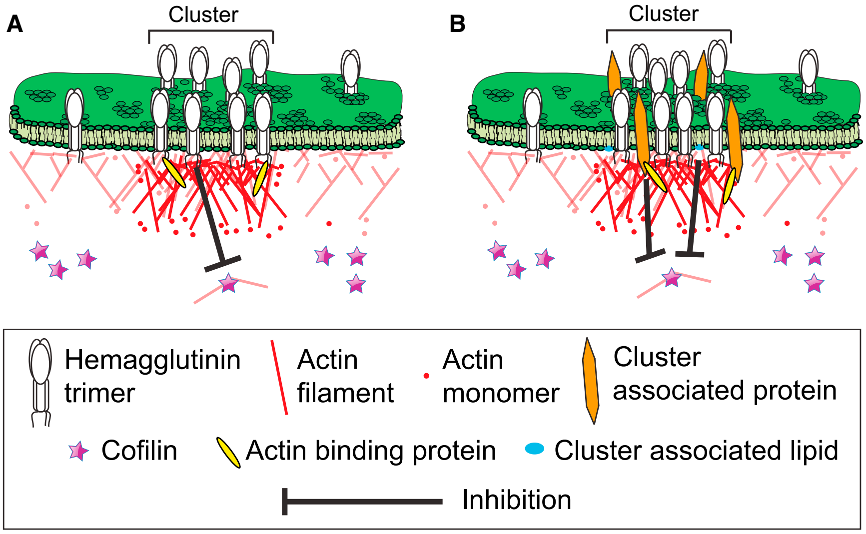

FIGURE 6 Cluster feedback. Models of actin-mediated organization of membrane proteins, and membrane protein-mediated organization of underlying actin. (*A*) HA signals to inactivate cofilin immediately adjacent to the plasma membrane, resulting in a higher local density of longer, more stable actin filaments. These filaments create a meshwork and increase the numbers of potential anchor points for HA molecules. Intermediate ABPs that may link actin filaments and HA proteins are unknown. Inverted black T indicates inhibition of cofilin. (*B*) HA clusters with other membrane-bound proteins and lipids, which themselves signal to inactivate cofilin locally. As in model *A*, this inactivation results in an increased local density of actin filaments and hence an increase in the number of anchor points for proteins in the cluster. Inverted black T indicates inhibition of cofilin.

between the two populations, and by the limited timescale over which HA trajectories can be obtained. Interestingly, the slow-moving HA fraction we observed could appear to be the immobile fraction in FRAP experiments. The finding that the slow-moving HA population is not completely immobile demonstrates that even within membrane regions that are highly concentrated with HA, and despite the strong correlation between HA and actin distributions, some lateral mobility is retained. Although it is consistent with predictions of anomalous lateral diffusion, the observation of HA mobility precludes the possibility that the HA molecules themselves serve as either immobile pickets in the membrane-associated fence, or that HA itself is bound directly to such immobile pickets.

Previous research has indicated the involvement of the G-protein-activated Src-family kinase Lyn in inducing periods of reduced mobility in clusters of GPI-anchored receptors (73). The cross-linking of GPI-anchored receptors also induces the formation of clusters on the order of hundreds of nanometers in size that colocalize with actin (41). It is unclear in our case whether HA acts to reorganize actin by directly initiating signaling cascades (Fig. 6 *A*) or indirectly through other regulators of actin organization (Fig. 6 *B*). Because cortical actin can mediate phase separation of membrane lipids (74,75), local enrichments in cortical actin may allow for a framework to which some membrane proteins can bind, while also stabilizing patches of certain lipids and proteins around these aggregations. Cell-surface accumulation and clustering of HA are known to activate PKCα and Raf/MEK/ERK pathways (25), both of which can regulate cofilin (63,76). Phosphatidylinositol bisphosphate (PIP$_2$) (4,5) is associated with each of these pathways (77,78) and is a regulator of cofilin activity (79). PIP$_2$ has also been implicated in mediating signaling from membrane domains to the cytoskeleton (80). Further work in which cofilin is imaged together with its regulators will help to elucidate the upstream pathways that ultimately control local cytoskeletal organization and its interactions with membrane components.

SUPPORTING MATERIAL

Six figures, one table, and supporting analysis are available at http://www.biophysj.org/biophysj/supplemental/S0006-3495(13)00426-8.

The authors thank J. Rochira, J. Bewersdorf, S. Bolduc, P. Blank, P. Wadsworth, S.R. McKay, A. DeCarlo, M. Parent, P. Andresen, P. Gunning, T. Fath, J. Bamburg, and R.D. Astumian for useful discussions; T. Tripp and D. Breton for machining, D. Bouchard, S. Ashworth, L. Hutchinson, R. Kennedy, M. Pietraszewski, R. Phennicie, J. Shim, K. Brothers, M. Mason, E. Allgeyer, and P. Millard for help with equipment and experiments; P. Byard for administrative assistance; and T. Schmidt and S. Semrau for the PICS analysis software and discussion.

This work was funded by the National Institutes of Health (NIH Career Award K25-AI65459, NIH R15-GM094713, NSF MRI CHE-0722759, and IGERT-0221625), the Maine Technology Institute (MTAF 1106 and 2061), UMaine V.P. for Research, the Maine Economic Improvement Fund (MEIF), and the Intramural Research Program of the National Institute of Child Health and Human Development. T.J.G. benefited from an MEIF doctoral dissertation fellowship. S.T.H. and T.J.G. hold patents in superresolution microscopy. S.T.H. serves on the scientific advisory board of Vutara, Inc.

REFERENCES

1. Anderson, R. G. W., and K. Jacobson. 2002. A role for lipid shells in targeting proteins to caveolae, rafts, and other lipid domains. *Science.* 296:1821–1825.
2. Jacobson, K., O. G. Mouritsen, and R. G. Anderson. 2007. Lipid rafts: at a crossroad between cell biology and physics. *Nat. Cell Biol.* 9:7–14.
3. Feder, T. J., I. Brust-Mascher, …, W. W. Webb. 1996. Constrained diffusion or immobile fraction on cell surfaces: a new interpretation. *Biophys. J.* 70:2767–2773.
4. Elson, E. L., J. Schlessinger, …, W. W. Webb. 1976. Measurement of lateral transport on cell surfaces. *Prog. Clin. Biol. Res.* 9:137–147.
5. Sako, Y., and A. Kusumi. 1995. Barriers for lateral diffusion of transferrin receptor in the plasma membrane as characterized by receptor dragging by laser tweezers: fence versus tether. *J. Cell Biol.* 129:1559–1574.
6. Fujiwara, T., K. Ritchie, …, A. Kusumi. 2002. Phospholipids undergo hop diffusion in compartmentalized cell membrane. *J. Cell Biol.* 157:1071–1081.
7. Sheetz, M. P. 1983. Membrane skeletal dynamics: role in modulation of red cell deformability, mobility of transmembrane proteins, and shape. *Semin. Hematol.* 20:175–188.
8. Chichili, G. R., and W. Rodgers. 2007. Clustering of membrane raft proteins by the actin cytoskeleton. *J. Biol. Chem.* 282:36682–36691.
9. Goswami, D., K. Gowrishankar, …, S. Mayor. 2008. Nanoclusters of GPI-anchored proteins are formed by cortical actin-driven activity. *Cell.* 135:1085–1097.
10. Holowka, D., E. D. Sheets, and B. Baird. 2000. Interactions between Fc(ε)RI and lipid raft components are regulated by the actin cytoskeleton. *J. Cell Sci.* 113:1009–1019.
11. Villalba, M., K. Bi, …, A. Altman. 2001. Vav1/Rac-dependent actin cytoskeleton reorganization is required for lipid raft clustering in T cells. *J. Cell Biol.* 155:331–338.
12. Jordan, S., and W. Rodgers. 2003. T cell glycolipid-enriched membrane domains are constitutively assembled as membrane patches that translocate to immune synapses. *J. Immunol.* 171:78–87.
13. Chichili, G. R., and W. Rodgers. 2009. Cytoskeleton-membrane interactions in membrane raft structure. *Cell. Mol. Life Sci.* 66:2319–2328.
14. Jaqaman, K., H. Kuwata, …, S. Grinstein. 2011. Cytoskeletal control of CD36 diffusion promotes its receptor and signaling function. *Cell.* 146:593–606.
15. Viola, A., and N. Gupta. 2007. Tether and trap: regulation of membrane-raft dynamics by actin-binding proteins. *Nat. Rev. Immunol.* 7:889–896.
16. Sheetz, M. P., J. E. Sable, and H.-G. Döbereiner. 2006. Continuous membrane-cytoskeleton adhesion requires continuous accommodation to lipid and cytoskeleton dynamics. *Annu. Rev. Biophys. Biomol. Struct.* 35:417–434.
17. Weigel, A. V., B. Simon, …, D. Krapf. 2011. Ergodic and nonergodic processes coexist in the plasma membrane as observed by single-molecule tracking. *Proc. Natl. Acad. Sci. USA.* 108:6438–6443.
18. Kenworthy, A. K., B. J. Nichols, …, J. Lippincott-Schwartz. 2004. Dynamics of putative raft-associated proteins at the cell surface. *J. Cell Biol.* 165:735–746.
19. White, J., A. Helenius, and M. J. Gething. 1982. Haemagglutinin of influenza virus expressed from a cloned gene promotes membrane fusion. *Nature.* 300:658–659.

20. Ellens, H., J. Bentz, …, J. M. White. 1990. Fusion of influenza hemagglutinin-expressing fibroblasts with glycophorin-bearing liposomes: role of hemagglutinin surface density. *Biochemistry.* 29:9697–9707.
21. Chen, B. J., G. P. Leser, …, R. A. Lamb. 2007. Influenza virus hemagglutinin and neuraminidase, but not the matrix protein, are required for assembly and budding of plasmid-derived virus-like particles. *J. Virol.* 81:7111–7123.
22. Takeda, M., G. P. Leser, …, R. A. Lamb. 2003. Influenza virus hemagglutinin concentrates in lipid raft microdomains for efficient viral fusion. *Proc. Natl. Acad. Sci. USA.* 100:14610–14617.
23. Shaw, M. L., K. L. Stone, …, P. Palese. 2008. Cellular proteins in influenza virus particles. *PLoS Pathog.* 4:e1000085.
24. Simpson-Holley, M., D. Ellis, …, P. Digard. 2002. A functional link between the actin cytoskeleton and lipid rafts during budding of filamentous influenza virions. *Virology.* 301:212–225.
25. Marjuki, H., M. I. Alam, …, S. Pleschka. 2006. Membrane accumulation of influenza A virus hemagglutinin triggers nuclear export of the viral genome via protein kinase Cα-mediated activation of ERK signaling. *J. Biol. Chem.* 281:16707–16715.
26. Hess, S. T., T. J. Gould, …, J. Zimmerberg. 2007. Dynamic clustered distribution of hemagglutinin resolved at 40 nm in living cell membranes discriminates between raft theories. *Proc. Natl. Acad. Sci. USA.* 104:17370–17375.
27. Hess, S. T., M. Kumar, …, J. Zimmerberg. 2005. Quantitative electron microscopy and fluorescence spectroscopy of the membrane distribution of influenza hemagglutinin. *J. Cell Biol.* 169:965–976.
28. Hess, S. T., T. P. K. Girirajan, and M. D. Mason. 2006. Ultra-high resolution imaging by fluorescence photoactivation localization microscopy. *Biophys. J.* 91:4258–4272.
29. Gould, T. J., M. S. Gunewardene, …, S. T. Hess. 2008. Nanoscale imaging of molecular positions and anisotropies. *Nat. Methods.* 5:1027–1030.
30. Subach, F. V., G. H. Patterson, …, V. V. Verkhusha. 2009. Photoactivatable mCherry for high-resolution two-color fluorescence microscopy. *Nat. Methods.* 6:153–159.
31. Sambrook, J., L. Rodgers, …, M. J. Gething. 1985. Lines of BPV-transformed murine cells that constitutively express influenza virus hemagglutinin. *EMBO J.* 4:91–103.
32. Gunewardene, M. S., F. V. Subach, …, S. T. Hess. 2011. Superresolution imaging of multiple fluorescent proteins with highly overlapping emission spectra in living cells. *Biophys. J.* 101:1522–1528.
33. Sneath, P. H. 1957. The application of computers to taxonomy. *J. Gen. Microbiol.* 17:201–226.
34. Greenfield, D., A. L. McEvoy, …, J. Liphardt. 2009. Self-organization of the Escherichia coli chemotaxis network imaged with super-resolution light microscopy. *PLoS Biol.* 7:e1000137.
35. Semrau, S., and T. Schmidt. 2007. Particle image correlation spectroscopy (PICS): retrieving nanometer-scale correlations from high-density single-molecule position data. *Biophys. J.* 92:613–621.
36. Gower, J. C., and G. J. S. Ross. 1969. Minimum spanning trees and single linkage cluster analysis. *J. R. Stat. Soc. Ser. C Appl. Stat*. 18:54–64.
37. Coué, M., S. L. Brenner, …, E. D. Korn. 1987. Inhibition of actin polymerization by latrunculin A. *FEBS Lett.* 213:316–318.
38. Brown, S. S., and J. A. Spudich. 1979. Cytochalasin inhibits the rate of elongation of actin filament fragments. *J. Cell Biol.* 83:657–662.
39. Bubb, M. R., A. M. J. Senderowicz, …, E. D. Korn. 1994. Jasplakinolide, a cytotoxic natural product, induces actin polymerization and competitively inhibits the binding of phalloidin to F-actin. *J. Biol. Chem.* 269:14869–14871.
40. Veatch, S. L., B. B. Machta, …, B. A. Baird. 2012. Correlation functions quantify super-resolution images and estimate apparent clustering due to over-counting. *PLoS ONE.* 7:e31457.
41. Sengupta, P., T. Jovanovic-Talisman, …, J. Lippincott-Schwartz. 2011. Probing protein heterogeneity in the plasma membrane using PALM and pair correlation analysis. *Nat. Methods.* 8:969–975.
42. Bamburg, J. R. 1999. Proteins of the ADF/cofilin family: essential regulators of actin dynamics. *Annu. Rev. Cell Dev. Biol.* 15:185–230.
43. Bernstein, B. W., and J. R. Bamburg. 2010. ADF/cofilin: a functional node in cell biology. *Trends Cell Biol.* 20:187–195.
44. Andrianantoandro, E., and T. D. Pollard. 2006. Mechanism of actin filament turnover by severing and nucleation at different concentrations of ADF/cofilin. *Mol. Cell.* 24:13–23.
45. Arber, S., F. A. Barbayannis, …, P. Caroni. 1998. Regulation of actin dynamics through phosphorylation of cofilin by LIM-kinase. *Nature.* 393:805–809.
46. Bernard, O. 2007. Lim kinases, regulators of actin dynamics. *Int. J. Biochem. Cell Biol.* 39:1071–1076.
47. Borisy, G. G., and T. M. Svitkina. 2000. Actin machinery: pushing the envelope. *Curr. Opin. Cell Biol.* 12:104–112.
48. Carlier, M.-F., V. Laurent, …, D. Pantaloni. 1997. Actin depolymerizing factor (ADF/cofilin) enhances the rate of filament turnover: implication in actin-based motility. *J. Cell Biol.* 136:1307–1322.
49. Endo, M., K. Ohashi, and K. Mizuno. 2007. LIM kinase and slingshot are critical for neurite extension. *J. Biol. Chem.* 282:13692–13702.
50. Endo, M., K. Ohashi, …, K. Mizuno. 2003. Control of growth cone motility and morphology by LIM kinase and Slingshot via phosphorylation and dephosphorylation of cofilin. *J. Neurosci.* 23:2527–2537.
51. Ghosh, M., X. Song, …, J. S. Condeelis. 2004. Cofilin promotes actin polymerization and defines the direction of cell motility. *Science.* 304:743–746.
52. Gu, J., C. W. Lee, …, J. Q. Zheng. 2010. ADF/cofilin-mediated actin dynamics regulate AMPA receptor trafficking during synaptic plasticity. *Nat. Neurosci.* 13:1208–1215.
53. Gungabissoon, R. A., and J. R. Bamburg. 2003. Regulation of growth cone actin dynamics by ADF/cofilin. *J. Histochem. Cytochem.* 51:411–420.
54. Kiuchi, T., K. Ohashi, …, K. Mizuno. 2007. Cofilin promotes stimulus-induced lamellipodium formation by generating an abundant supply of actin monomers. *J. Cell Biol.* 177:465–476.
55. Kuhn, T. B., P. J. Meberg, …, J. R. Bamburg. 2000. Regulating actin dynamics in neuronal growth cones by ADF/cofilin and rho family GTPases. *J. Neurobiol.* 44:126–144.
56. McGough, A., B. Pope, …, A. Weeds. 1997. Cofilin changes the twist of F-actin: implications for actin filament dynamics and cellular function. *J. Cell Biol.* 138:771–781.
57. Minamide, L. S., W. B. Painter, …, J. R. Bamburg. 1997. Differential regulation of actin depolymerizing factor and cofilin in response to alterations in the actin monomer pool. *J. Biol. Chem.* 272:8303–8309.
58. Nakano, K., and I. Mabuchi. 2006. Actin-depolymerizing protein Adf1 is required for formation and maintenance of the contractile ring during cytokinesis in fission yeast. *Mol. Biol. Cell.* 17:1933–1945.
59. Nishimura, Y., K. Yoshioka, …, K. Itoh. 2006. A role of LIM kinase 1/cofilin pathway in regulating endocytic trafficking of EGF receptor in human breast cancer cells. *Histochem. Cell Biol.* 126:627–638.
60. Okreglak, V., and D. G. Drubin. 2007. Cofilin recruitment and function during actin-mediated endocytosis dictated by actin nucleotide state. *J. Cell Biol.* 178:1251–1264.
61. Pawlak, G., and D. M. Helfman. 2002. MEK mediates v-Src-induced disruption of the actin cytoskeleton via inactivation of the Rho-ROCK-LIM kinase pathway. *J. Biol. Chem.* 277:26927–26933.
62. Rosso, S., F. Bollati, …, A. Cáceres. 2004. LIMK1 regulates Golgi dynamics, traffic of Golgi-derived vesicles, and process extension in primary cultured neurons. *Mol. Biol. Cell.* 15:3433–3449.
63. Sakuma, M., Y. Shirai, …, N. Saito. 2012. Novel PKCα-mediated phosphorylation site(s) on cofilin and their potential role in terminating histamine release. *Mol. Biol. Cell.* 23:3707–3721.
64. Sarmiere, P. D., and J. R. Bamburg. 2004. Regulation of the neuronal actin cytoskeleton by ADF/cofilin. *J. Neurobiol.* 58:103–117.

65. Wang, W., G. Mouneimne, …, J. S. Condeelis. 2006. The activity status of cofilin is directly related to invasion, intravasation, and metastasis of mammary tumors. *J. Cell Biol.* 173:395–404.

66. Yang, N., O. Higuchi, …, K. Mizuno. 1998. Cofilin phosphorylation by LIM-kinase 1 and its role in Rac-mediated actin reorganization. *Nature.* 393:809–812.

67. Pollard, T. D., and G. G. Borisy. 2003. Cellular motility driven by assembly and disassembly of actin filaments. *Cell.* 112:453–465.

68. Verkhovsky, A. B., O. Y. Chaga, …, G. G. Borisy. 2003. Orientational order of the lamellipodial actin network as demonstrated in living motile cells. *Mol. Biol. Cell.* 14:4667–4675.

69. Chen, H., B. W. Bernstein, and J. R. Bamburg. 2000. Regulating actin-filament dynamics in vivo. *Trends Biochem. Sci.* 25:19–23.

70. Su, B., Y. Bu, …, I. H. Gelman. 2010. SSeCKS/Gravin/AKAP12 inhibits cancer cell invasiveness and chemotaxis by suppressing a protein kinase C-Raf/MEK/ERK pathway. *J. Biol. Chem.* 285:4578–4586.

71. Larsson, C. 2006. Protein kinase C and the regulation of the actin cytoskeleton. *Cell. Signal.* 18:276–284.

72. Engel, S., S. Scolari, …, M. Veit. 2010. FLIM-FRET and FRAP reveal association of influenza virus haemagglutinin with membrane rafts. *Biochem. J.* 425:567–573.

73. Suzuki, K. G., T. K. Fujiwara, …, A. Kusumi. 2007. GPI-anchored receptor clusters transiently recruit Lyn and G α for temporary cluster immobilization and Lyn activation: single-molecule tracking study 1. *J. Cell Biol.* 177:717–730.

74. Liu, A. P., and D. A. Fletcher. 2006. Actin polymerization serves as a membrane domain switch in model lipid bilayers. *Biophys. J.* 91:4064–4070.

75. Baumgart, T., A. T. Hammond, …, W. W. Webb. 2007. Large-scale fluid/fluid phase separation of proteins and lipids in giant plasma membrane vesicles. *Proc. Natl. Acad. Sci. USA.* 104:3165–3170.

76. Nebl, G., S. Fischer, …, Y. Samstag. 2004. Dephosphorylation of cofilin is regulated through Ras and requires the combined activities of the Ras-effectors MEK and PI3K. *Cell. Signal.* 16:235–243.

77. Lopez, C. I., L. E. Pelletán, …, S. A. Belmonte. 2012. Diacylglycerol stimulates acrosomal exocytosis by feeding into a PKC- and PLD1-dependent positive loop that continuously supplies phosphatidylinositol 4,5-bisphosphate. *Biochim. Biophys. Acta.* 1821:1186–1199.

78. Garrenton, L. S., C. J. Stefan, …, J. Thorner. 2010. Pheromone-induced anisotropy in yeast plasma membrane phosphatidylinositol-4,5-bisphosphate distribution is required for MAPK signaling. *Proc. Natl. Acad. Sci. USA.* 107:11805–11810.

79. Yonezawa, N., E. Nishida, …, H. Sakai. 1990. Inhibition of the interactions of cofilin, destrin, and deoxyribonuclease I with actin by phosphoinositides. *J. Biol. Chem.* 265:8382–8386.

80. Johnson, C. M., and W. Rodgers. 2008. Spatial segregation of phosphatidylinositol 4,5-bisphosphate (PIP(2)) signaling in immune cell functions. *Immunol. Endocr. Metab. Agents Med. Chem.* 8:349–357.

SUPPORTING MATERIAL

for

"Actin Mediates the Nanoscale Membrane Organization of the Clustered Membrane Protein Influenza Hemagglutinin"

Manasa V. Gudheti,[1,2*] Nikki M. Curthoys,[1*] Travis J. Gould,[1,3] Dahan Kim,[1] Mudalige S. Gunewardene,[1] Kristin A. Gabor,[1,4,5] Julie A. Gosse,[4,5] Carol H. Kim,[4,5] Joshua Zimmerberg,[6] and Samuel T. Hess[1,5†]

[1] Department of Physics and Astronomy, 120 Bennett Hall,
University of Maine, Orono, ME 04469, USA

[2] Current address: Department of Biology, University of Utah; and Vutara, Inc., 615 Arapeen #304, Salt Lake City, UT 84108, USA

[3] Current address: Department of Cell Biology, Yale University School of Medicine, New Haven, 333 Cedar Street, CT 06510, USA

[4] Department of Molecular and Biomedical Sciences, 5735 Hitchner Hall, University of Maine, Orono, ME 04469, USA

[5] Graduate School of Biomedical Sciences, 263 ESRB/Barrows Hall, University of Maine, Orono, ME 04469, USA

[6] Program in Physical Biology, Eunice Kennedy Shriver National Institute of Child Health and Human Development, National Institutes of Health, Bethesda, MD 20892, USA

*** these authors contributed equally**

Running Title: Actin and Membrane Organization of HA

† Corresponding author. Present address: 313 Bennett Hall, Department of Physics and Astronomy, University of Maine, Orono, ME 04469. Phone: 207 581-1036. Fax: 207 581-3410. Email: sam.hess@umit.maine.edu

Preparation for Imaging. NIH3T3-HAb2 cells were grown in DMEM (with serum but without phenol red or antibiotics) to ~80% confluence in eight-well coverglass chambers (#1.5, Nalge Nunc) for room temperature (RT) imaging. NIH3T3-HAb2 cells were grown in 35 mm glass bottom dishes (P35G-1.5-20-C, MatTek Corporation, Ashland, MA) to ~80% confluence for 37°C live cell imaging. Using Lipofectamine 2000 (Lipo) (Invitrogen) according to the manufacturer's procedures, cells in eight-well coverglass chambers were transfected with ~1 µg DNA per well of Dendra2-HA (1) and/or PAmCherry-actin (2) or PAmCherry-cofilin in reduced-serum media (Opti-MEM, Gibco/Invitrogen) without antibiotics. When transfecting cells plated in 35 mm dishes, ~5 µg of DNA of each construct was used. Cells were then grown for an additional 24–30 h in the presence of serum supplemented media without phenol red. For fixation, cells were rinsed three times in PBS, incubated for ~20 - 30 min in 4% paraformaldehyde (PFA, USB Corporation, Cleveland, OH) in PBS at RT, and rinsed three more times with UV-bleached PBS to reduce background from fluorescent contaminants (1, 3).

For two-color live cell imaging, the following DNA/Lipo ratios were used for transfecting: Dendra2-HA (0.52 µg DNA/µL Lipo), PAmCherry-actin (0.4-0.5 µg DNA/µL Lipo), and PAmCherry-cofilin (0.5 µg DNA/µL Lipo) were found to be optimal. For a single transfection in 35 mm dishes, 5 µL of Lipo and the appropriate amount of DNA were added to separate aliquots (250 µL) of Opti-MEM. The manufacturer's protocol was followed and thereafter the transfection media was replaced after ~5 h of transfection with growth media containing antibiotics but no phenol red. Cells were rinsed three times and imaged with low background Dulbecco's phosphate-buffered saline (DPBS) containing calcium and magnesium (BioWhittaker Lonza, Walkersville, MD) supplemented with 10 mM glucose 30 hours post-transfection. The low background level of the buffer rendered it suitable for FPALM imaging without the need for UV bleaching.

Actin Cytoskeleton Disruption. For disrupting the actin cytoskeleton, plated NIH3T3- HAb2 cells were grown to ~40-50% confluence in DMEM with serum, without phenol red and with antibiotics and then transfected as above. Approximately 30 hours post-transfection the cells were incubated with actin disrupters at 37°C and 5% CO2. Stock solutions of latrunculin A (LatA) (Sigma–Aldrich, St. Louis, MO), cytochalasin D (CytoD) (Sigma–Aldrich) and jasplakinolide (Jas) (Sigma–Aldrich) were made in DMSO (Fluka). The initial master stocks (dissolved in DMSO) were diluted in sterile PBS to achieve a working stock of 1 mM. DMSO diluted in sterile PBS was added to the control sample to mimic the volume percent (0.01%) of DMSO present in each of the drug treatments. NIH3T3-HAb2 cells were incubated with full growth media supplemented with 1 µM LatA for 10 minutes, 1 µM CytoD for 60 minutes, 1 µM Jas for 30 minutes and 0.01% DMSO (Control) for 60 minutes. Subsequently the cells were rinsed 3 times with UV-bleached PBS and fixed in 4% PFA in PBS at RT for 20 minutes before being rinsed a further 3 times and imaged in UV-bleached PBS.

*Alexa 488 Phalloidin Staining to Visualize F-actin Expression***.** Alexa Fluor 488 phalloidin (referred to as Alexa 488 phalloidin throughout) (Life Technologies, Invitrogen) was used to investigate the effects of LatA, CytoD, and Jas on F-actin in NIH3T3-HAb2 cells. Cells were plated onto eight-well coverglass chambers (#1.5, Nalge Nunc) in DMEM, with serum, without phenol red and with antibiotics to ~80% confluence. After subjecting NIH3T3-HAb2 cells to the corresponding treatments the cells were rinsed twice with PBS, fixed at RT for 10 minutes with 4% PFA, rinsed twice again with PBS and permeabilized at RT with 0.01% Triton X-100

(Sigma-Aldrich) in PBS for 4 minutes. The cells were again rinsed twice with PBS and incubated with 1% bovine serum albumin (BSA, Sigma-Aldrich) in PBS for 20 minutes at RT to block non-specific labeling. Thereafter, Alexa 488 phalloidin (Life Technologies, Invitrogen) diluted 1 in 200 into PBS with 0.5% BSA was added to the cells for 20 minutes at RT. PBS was then used to rinse the cells three times and was subsequently used as the imaging media. Alexa Fluor 680 phalloidin (Life Technologies, Invitrogen) was used to compare the distributions of endogenous filamentous actin and transiently transfected Dendra2-HA in NIH3T3-HAb2 cells. The above protocol was used, except that Alexa 680 phalloidin was diluted 1 in 100 in PBS only.

Single-Color FPALM Imaging and Analysis

Single-color FPALM imaging and analysis was performed as described earlier (3-5). A 405 nm diode laser (BCL-405-15, Crystalaser, Reno, NV) was used to activate photoactivatable molecules in the sample, while either a 556 nm (LRS-556-NM-100-10, Laserglow, Toronto, Canada) or a 555 nm (GCL-100-555-M, Crystalaser) diode laser was used to readout active molecules. Both beams were focused at the back aperture of a 60X / 1.2 NA water-immersion objective lens (UPLAPO60XW, Olympus, Melville, NY) to produce widefield illumination at the sample. Fluorescence from the sample was collected by the same objective, separated from laser light by a dichroic mirror (T565LP, Chroma Technology, Rockingham, VT), bandpass filtered (ET605/70M, Chroma Technology), and imaged by an EMCCD camera (iXon+ DU897DCS-BV, Andor Scientific, Belfast, Ireland) operated at EM gain of 200 and frame rates of either ~31.5, 46.0, 59.7, or 69.8 Hz. The camera was controlled using Solis software (Andor). Additional achromatic lenses (f=+60 mm and f=+200 mm, Newport Corporation, Irvine, CA) arranged as a telescope were mounted in the detection path to provide additional magnification and produce an effective camera pixel size of ~83 nm.

Similar to previously published methods, (3) readout laser intensities ranged from ~10^3–10^4 W/cm^2. For activation, continuous low-intensity 405 nm illumination was used with intensities ranging from 0–10^2 W/cm^2. A motorized filter wheel (FW102, Thorlabs, Newton, NJ) containing neutral density filters provided manual incrementing of the activation intensity in steps of $10^{0.5}$ to maintain a density of visible molecules of ~1/μm^2.

Cells were selected for FPALM imaging by exciting the sample with a mercury lamp (excitation filter 475/40x, Chroma) and viewing, searching for green fluorescence (bandpass-filtered, HQ535/50M, Chroma) to locate cells transfected with Dendra2-HA. During post acquisition analysis, each frame of an image series (typically 5,000 – 20,000 frames total) was background subtracted and positive intensity peaks with at least one pixel above a minimum threshold were fitted to a two-dimensional Gaussian to determine the x and y coordinates, amplitude (I_0), e^{-2} radius (r_0), and an offset. Fitted values of I_0 and r_0 were then used to calculate the number of detected photons ($N = I_0 \pi r_0^2 / 2$). Fits that yielded N and r_0 consistent with that expected for a single molecule were recorded for further analysis. For each localized molecule the localization precision was calculated using the standard analytical equation from the literature, plus an additional 30% (6). Lateral drift of the sample stage was characterized previously (< 7 nm in x or y over ~20 min) (5) and was assumed to be negligible over the duration of these experiments, compared to the estimated lateral resolution of ~10-30 nm. All analysis was performed using custom software written in MATLAB (Mathworks, Natick, MA). Transmitted light images were also obtained post-acquisition using either a Quantifire (Optronics, Goleta, CA) or a Photometrics Cascade 512B (Roper Scientific, GmbH, Germany) camera mounted at an additional camera port of the microscope stand.

The high densities of HA measured by FPALM place a lower bound on the detection efficiency of labeled molecules. HA density observed in X-31 viral membranes is ~7000 HA trimers/μm^2, (7) or ~21x10^3 HA monomers/μm^2. Our observed densities in some NIH3T3-HAb2 cell clusters of ~ 6-7x10^3 trimers/μm^2 or 20x10^3 monomers/μm^2 suggest we have a high labeling and localization efficiency.

The three-dimensional membrane within the ±0.5 μm depth of field is imaged as a two-dimensional projection, which could introduce distortions in observed clusters. Based on electron microscopy serial sections of membrane sheets from NIH3T3-HAb2 cells (8), the three-dimensional topography of the membrane (maximum ~200 nm displacement in the axial direction) is calculated to affect molecular intensities and point spread function area by ~9% for a 200 nm axial displacement, which is not expected to affect FPALM localization efficiency, and is expected to affect localization precision by ~5%. Local sloping of the membrane could, however, influence (and generally increase) apparent molecular density, the effects of which we neglect.

Single-Color Live-cell FPALM

Temperature Control. For live-cell imaging, cells were maintained at 37 ±0.2 °C using a TC-202A temperature controller and PDMI-2 micro incubator stage (Harvard Apparatus, Holliston, MA) mounted to the stage of an inverted microscope (IX71, Olympus). The FPALM setup is the same as that used for single-color fixed-cell imaging.

Diffusion Analysis. To determine the mobility of HA, localized molecules in consecutive frames were tracked using a nearest-neighbor (NN) algorithm. For each molecule in the ith frame, the NN in the same frame and the two NNs in the (i+1)th frame were calculated. The first NN in the (i+1)th frame was linked to the molecule in the ith frame if the following criteria was satisfied. 1) the distance from the first NN in the (i+1)th frame was less than R_{max} (typically 300 nm), 2) the distance from second NN in the (i+1)th frame was greater than $2R_{max}$, and 3) the distance from the NN in the same frame was also greater than $2R_{max}$. Criteria 2) and 3) served to minimize errors in assignment of molecules. A trajectory was terminated when any criterion was not satisfied.

From identified trajectories, histograms of diffusion steps sizes were generated and fitted to a two-component model of diffusion. The probability that a diffusing molecule starting at the origin will be found within a circle of radius r at a later time Δt is described by the cumulative distribution function P(r,Δt). A two-component system in which fractions α and (1-α) of molecules are characterized by diffusion coefficients D_1 and D_2, respectively, is described by (9):

$$P(r,\Delta t)=\alpha(1-e^{-r^2/r_1^2})+(1-\alpha)(1-e^{-r^2/r_2^2}) \tag{1}$$

where r_i^2 are the mean-square displacements (MSDs), i.e. $r_i^2 = 4D_i\Delta t$ for free 2D diffusion. The probability of a diffusion step of length r is given by $p(r,\Delta t) = \partial P(r,\Delta t)/\partial r$:

$$p(r,\Delta t)=2\left(\frac{\alpha r}{r_1^2}e^{-r^2/r_1^2}+\frac{(1-\alpha)r}{r_2^2}e^{-r^2/r_2^2}\right). \tag{2}$$

Alternatively, particle image correlation spectroscopy (PICS) (10) was used to characterize diffusion using software obtained from the Schmidt lab. Briefly, the number of molecules localized in the (i+k)th frame within a distance r of a given molecule localized in the ith frame were tabulated to determine the cumulative correlation function, C(r,Δt):

$$C(r,\Delta t) = P(r,\Delta t) + c\pi r^2 \qquad (3)$$

where $P(r,\Delta t)$ is again the cumulative distribution function and the second terms accounts for the proximity to molecules on average. Values of $C(r,\Delta t)$ at longer distances were used to determine the average concentration (c) such that the second term could be subtracted from Eq. 4 to provide $P(r,\Delta t)$ which was again taken to be of the form of Eq. 2. Data was also corrected for undercounting due to diffraction and photobleaching (10). The frame delay, *k*, translates to a time- lag, $\Delta t = k\,'\,\tau_F$, where τ_F is the time per frame. Eq. 2 was then used to determine the fraction α and the MSDs of each population as a function of time-lag. For free 2D diffusion we expect the MSD to increase linearly with time-lag:

$$r_i^2 = 4D_i\Delta t + 2\sigma^2 \qquad (4)$$

where the finite localization precision (σ) results in a constant offset to the MSDs . MSDs which exhibited asymptotic behavior at longer time-lags were fit to a confined diffusion model. Confined diffusion within a square area L^2 with impermeable, reflecting boundaries is modeled by (11):

$$r_2^2(\Delta t) = \frac{L^2}{3}\left(1 - e^{-12D_0\Delta t/L^2}\right) \qquad (5)$$

where D_0 is the short length scale diffusion coefficient.

Turn Angle and Mobility Measurements. HA single molecule trajectories were analyzed to determine turn angle and mobility variations with respect to neighboring actin densities. The collected two-color FPALM data were initially sorted to identify each type of molecule (Dendra2-HA or PAmCherry-actin) based upon relative intensity ratios measured in each channel (transmitted (T), reflected (R)). A square grid spanning each imaged cell was defined with a grid box size of 0.2 x 0.2 μm^2. The number of actin molecules falling within each grid box was counted and actin density determined. For any two single molecule hops belonging to a given trajectory, the angle spanned from initial step direction towards the direction of subsequent step was defined as the turn angle. Based on the location of the origin on the density map of such an initial step in a HA trajectory, the corresponding local actin density was recorded along with the determined turn angle. The turn angles were next sorted with respect to local actin density (above or below median). Histograms of sorted turn angles were generated with turn angles spanning -180° to 180° with a 10° bin size. Turn angle histograms were further normalized with respect to the total turn angles measured to depict relative frequency of occurrence of a given turn angle in a high or low actin density region. In a strategically similar fashion the HA trajectory steps were used to determine the squared displacements for each step and keeping a record of neighboring actin density. Such squared displacements were binned with respect to actin density and for each bin the square displacements were averaged and divided by the time per step (31.75 ms at 31.5 Hz frame rate) to determine mobility. These measurements were used to generate HA mobility versus actin density plots.

Two-Color FPALM

Two-Color FPALM: Acquisition. These methods are described in detail in (12). In brief, two-color imaging on fixed NIH3T3-HAb2 cells was performed using the same setup as for single-color FPALM with the exception that a dichroic mirror and emission filters were mounted in the detection path between the telescope and the EMCCD camera, similar to a detection scheme used previously for multi color imaging (13). Although Dendra2 (peak emission 573 nm) and PAmCherry (peak emission 595 nm) have overlapping emission spectra, each probe can be identified by the ratio of emission in each detection channel as has been previously demonstrated with photoswitchable rhodamine derivatives (13). For two-color live-cell FPALM, cells were maintained at 37±0.2 °C using the same procedures as for single-color live-cell FPALM (see above). A 561 nm diode (Sapphire 561-100CW CDRH, Coherent, GmbH, Germany) readout laser and 405 nm diode (BCL-405-15, Crystalaser) activation laser were circularly polarized using a mounted achromatic quarter-wave plate (AQWP05M-600 Thorlabs, Newton, NJ) which is effective over the wavelength range of 400 - 800 nm. A custom-built 3X beam expander was used in front of the activation laser to further spread the beam. Widefield illumination at the sample was achieved by focusing both laser beams at the back aperture of a 60X / 1.2NA water-immersion objective lens (UPLAPO60XW, Olympus). Fluorescence from the sample was collected by the same objective, separated from the laser light by a dichroic mirror (T565LP, Chroma Technology), and long-pass filtered (LP02-561-RU-25, Semrock Inc., Rochester, NY), with both located in the same filter cube of the microscope. Fluorescence was then sent through a 405 nm notch filter (NF03-405E-25, Semrock Inc.) to cut off any activation laser bleed-through. Two additional lenses (f=+100 mm and f=+300 mm) (Thorlabs) were placed in the detection path to yield a roughly 3x magnification of the image formed on the sensor of an EMCCD camera (iXon+DU897DCS-BV, Andor Technology). After the last telescope lens and before the camera the detected light was split by a dichroic mirror (Z568RDC, Chroma Technology) such that reflected light was sent through one emission filter (ET605/70M, Chroma Technology) and transmitted light through another emission filter (FF01-630-92-25, Semrock Inc., Rochester, NY) with additional broadband dielectric mirrors placed to make split beam path lengths equal before forming separate images on two distinct regions of camera EMCCD. Images were acquired at EM gain of 200 and frame rates of ~31.5 Hz for 8000 frames. The readout laser power was ~5-10 kW/cm^2 and the activation power ranged from 0-10^2 W/cm^2 at the sample.

Before the start of each day of experiments (fixed and live cell two-color), images of fluorescent beads (TetraSpeck, Invitrogen) were obtained to correlate the two detection channels; with correlation done during post-acquisition analysis. Cells confirmed to express Dendra2-HA were then positioned to image the coverslip proximal membrane. Only cells which were later confirmed to express PAmCherry-actin (fixed- or live-cell) or PAmCherry-cofilin (fixed-cell only) by post-acquisition analysis were considered for further interpretation.

Two-Color FPALM: Analysis. This was an extension of the basic FPALM analysis described above and was used for both fixed and live cell imaging. As in other localization based techniques employing a split detection path (1, 13, 14), the raw frames now contained two spatially separated images (here representing the emission wavelengths transmitted and reflected by the dichroic mirror) which were correlated using transformation parameters (including translation, linear stretching, and rotation) obtained from the images of fluorescent beads (TetraSpeck, Invitrogen) and then superimposed for the standard localization routine. For each localized molecule the intensity in each detection channel was calculated as the sum of the pixel intensities in a 5x5 pixel box centered about the pixel containing the localized coordinates of the molecule. Intensity ratio of transmitted to the sum of the transmitted and reflected light was then calculated to produce a histogram of these values (α-values) between 0 and 1 from which the identity of the probe was identified (see 12 for more detail). Each localized molecule was assigned as either a Dendra2-tagged (HA) or PAmCherry-tagged (cofilin or actin, depending on the experiment) if its calculated ratio lied within the respective range of α-values chosen such that the error in assignment to either species was < 5%. For trajectory analysis of two-color live-cell imaging: after identification, each species (color) was analyzed separately using the same procedure used for the single-color diffusion analysis.

Statistical Analysis of Clustering

Pair Correlation. Coordinates of individual molecules obtained from FPALM imaging were used to calculate pair correlation functions. Localizations of the same molecules in consecutive frames were removed from the data set by linking molecules in the i^{th} frame to molecules in the $(i+1)^{th}$ frame that were separated by less than 3 times the median localization precision. The positions of linked molecules were then averaged for use in pair correlation calculations. The correlation, g(r), of species A with species B was calculated from:

$$g(r) = \frac{1}{n_A} \sum_{i=1}^{n_A} n_B(r_i) / (A_r \rho_B) \qquad (6)$$

where $n_B(r_i)$ is the number of molecules of species B that within a 10 nm-thick shell of radius r from the i^{th} molecule of species A; A_r is the area of the shell; n_A is total number of species A used in the summation, and ρ_B is the average density (number per unit area) of species B. So that edge correction was not required, the summation was only performed for molecules of species A that were less than the maximum distance used in the calculation (typically 1 µm) from the edge of a cell. Values of $g(r) > 1$ indicate correlation between species while $g(r) < 1$ indicates anti-correlation. For uniform distribution of molecules, $g(r) = 1$ is expected. Calculated values of g(r) were fitted to the analytical correlation function (15):

$$g(r) = Ce^{-r/r_0} / r^{\eta} \qquad (7)$$

including a constant offset, where A is the amplitude, r_0 is the correlation length, η and is a number.

Bleed-Through Correction of Pair Correlation

For calculation of cross pair-correlation values, localized molecules within a chosen mask of a two-color FPALM image were identified for their probe species by their α-values, by selecting α-value ranges for Dendra2 (channel A) and PAmCherry (channel B) and discarding molecules in the range of α with a high overlap between Dendra2 and PAmCherry distributions. For each probe species, these selected, localized molecules were then projected onto a grid to obtain two density plots, one for each probe, whose pixel values equal the number of molecules localized within each respective grid element. These density plots were then corrected for the bleed-through according to the bleed-through rates determined from α-value histograms of single-species samples for the defined α-value ranges for Dendra2 and PAmCherry, using

$$n_A^{corr} = \frac{n_A^{meas} - k_{BA} n_A^{meas} - k_{BA} n_B^{meas}}{1 - k_{AB} - k_{BA}} \qquad (8)$$

and

$$n_B^{corr} = \frac{n_B^{meas} - k_{AB} n_A^{meas} - k_{AB} n_B^{meas}}{1 - k_{AB} - k_{BA}} \qquad (9)$$

where n_A^{corr} and n_B^{corr} are the corrected A and B channel pixel values, respectively, n_A^{meas} and n_B^{meas} are the measured A and B pixel values, respectively, k_{AB} is the per-molecule bleed-through rate of channel A (Dendra2) into channel B (PAmCherry), and k_{BA} is the per-molecule bleed-through rate of channel B into channel A. For each non-zero pixel in the Dendra2 density plot after the bleed-through correction, the sum of PAmCherry density-plot pixel values was calculated for all the pixels whose centers were at a radius r ± Δr/2, then normalized:

$$g_{AB}(r) = \frac{1}{N_A^{corr}} \sum_i \sum_j \; n_A^{icorr} n_B^{jcorr} (r \pm \Delta r/2) \Big/ (A(r)\rho_B^{corr}) \tag{10}$$

where i is an index running over all pixels, j is an index running over all pixels at a radius r±Δr/2 from the ith pixel, N_A^{corr} is the total number of species A corrected for bleed-through, A(r) is the sum of areas of all pixels that have centers within r±Δr/2 of the i^{th} pixel, n_A^{icorr} is the number of species A in the i^{th} pixel, n_B^{jcorr} is the number of species B in the j^{th} pixel, corrected for bleed-through, and ρ_B^{corr} is the average density of species B (number per unit area) corrected for bleed-through. The average density was obtained using a mask drawn manually around the given cell being analyzed. The value of g_{AB} is computed for values of r ranging from 0 to a maximum r in steps of Δr. This radial distribution of PAmCherry with respect to a single Dendra2 density-plot pixel is then weighted by the value of the Dendra2 density-plot pixel for which the radial distribution is calculated, and was computed only for Dendra2 density-plot pixels that were at a minimum distance r inward from the region of interest mask to avoid edge effects. The average of this distribution for all non-zero Dendra2 density-plot pixels was reported as the radial distribution, or the pair-correlation, between Dendra2 and PAmCherry, after another normalization by the average density of PAmCherry molecules over the masked area. This method of pair-correlation calculation is identical to the calculation using the standard definition for pair-correlation, but is done on the basis of grid elements that allow correction of bleed-through. For our calculations, we used 0.2-0.58 for the range of α-values of Dendra2, 0.65-1.0 for the range of α-values of PAmCherry, k_{AB}=0.0463, k_{BA}=0.0496, grid pixel size of 0.01μm, Δr = 0.01μm, and maximum *r* of 1.00μm.

Table S1. Effects of Actin Disrupting Drugs on HA Cluster Area and Density in Fixed NIH3T3-HAb2 Cells

	Control **(n = 25 cells)**[*]	**LatA** **(n = 34 cells)**[*]	**CytoD** **(n = 17 cells)**[*]	**Jas** **(n = 23 cells)**[*]
Area (μm^2)[†]	0.151±0.006	0.154±0.006	0.274±0.015	0.213±0.012
Difference to control[‡]		$p > 0.05$	$p < 0.0001$	$p < 0.05$
Density (# of HA/μm^2)[†]	3670±120	3260±60	2720±80	3910±230
Difference to control[‡]		$p < 0.05$	$p < 0.0001$	$p > 0.05$

[*] Clusters analyzed contained at least 200 HA proteins

[†] Means±SEM of HA cluster areas and densities from the stated number of cells measured on at least two different days (typically three), with an average of ~14.8 clusters analyzed per cell

[‡] Statistical significance was determined with Prism (Graphpad, San Diego, CA, USA) as determined by one-way ANOVA with a Tukey's post test.

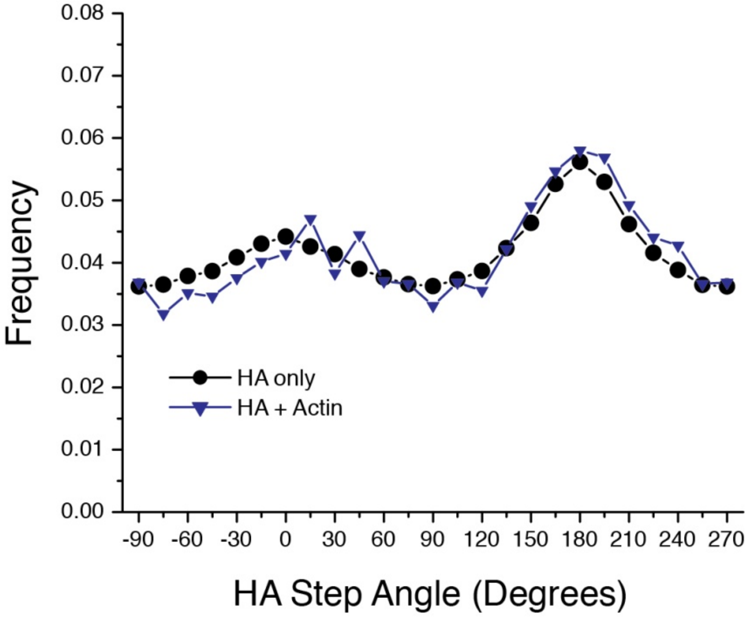

Figure S1. Comparison of HA turn angle histograms with and without PAmCherry-Actin. We imaged Dendra2-HA with FPALM in live cells expressing Dendra2-HA only (black dots), and compared with HA dynamics in live cells expressing both Dendra2-HA and PAmCherry actin (blue triangles), in regions where the PAmCherry-actin was present at low (below median) levels. Since our other results show that HA mobility is strongly affected by actin (Fig. 2), we expect to find that cell regions with high levels of PAmCherry-actin will show different mobility compared to cell regions with low levels of PAmCherry-actin (Fig. 2). Rather, to test for non-specific effects of the expression of PAmCherry-actin, we consider regions with below median levels of PAmCherry-actin, but in cells which have both Dendra2-HA and PAmCherry-actin, and compare with cells which have only Dendra2-HA. Note that the histograms are both normalized to a total area of 1.

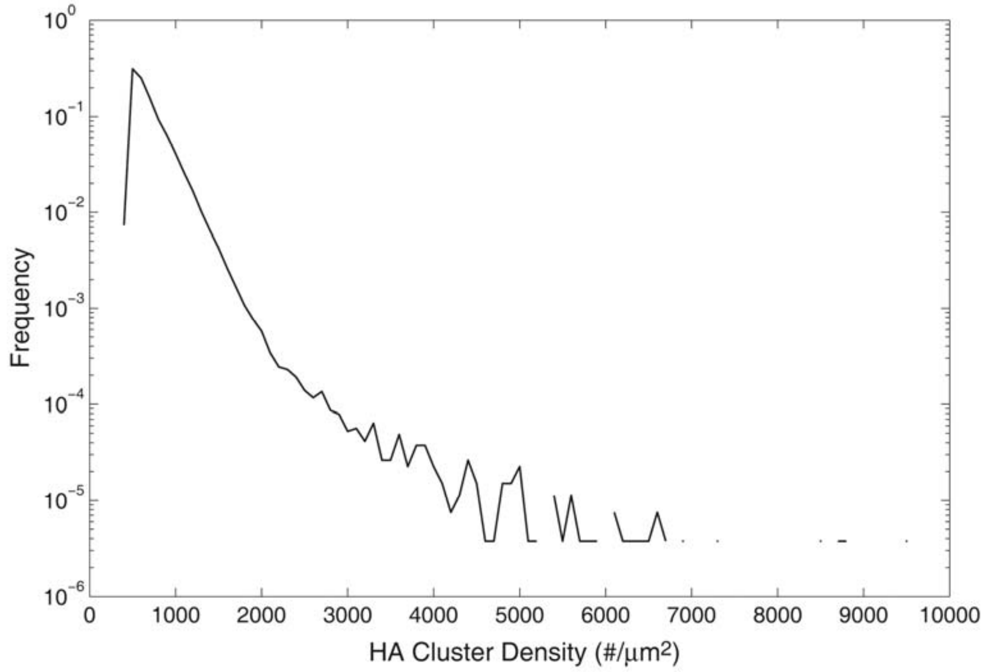

Figure S2. Histogram of HA cluster density in untreated, fixed NIH3T3-HAB2 cells (n=57 cells) expressing Dendra2-HA imaged by FPALM. The histogram has been normalized to a total area of unity and includes all clusters identified by single linkage cluster analysis with a maximum HA nearest neighbor distance of 30 nm. Note the considerable range in cluster densities. Gaps in the line indicate zeros in the histogram.

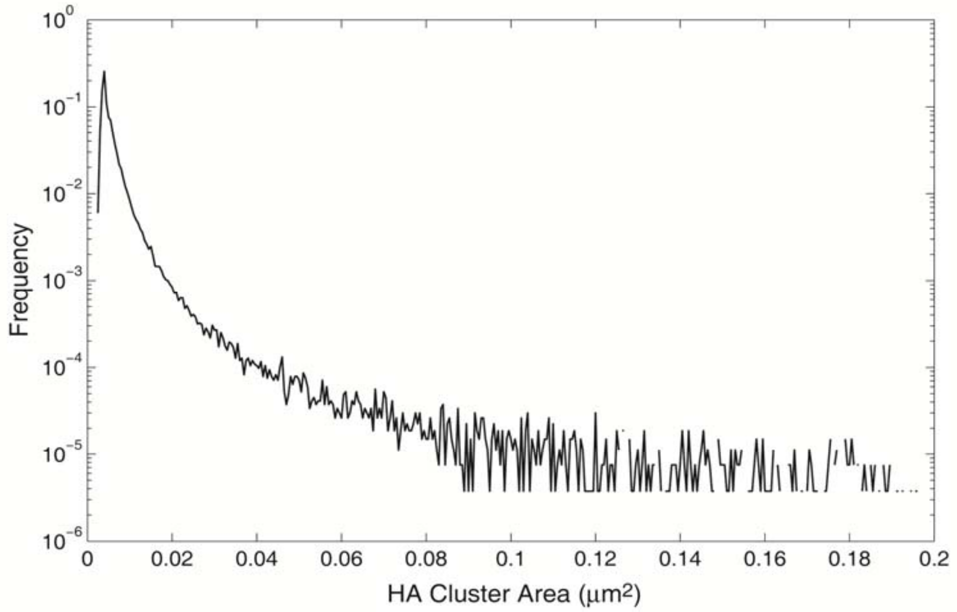

Figure S3. Histogram of HA cluster area in untreated, fixed NIH3T3-HAB2 cells (n=57 cells) expressing Dendra2-HA imaged by FPALM. The histogram has been normalized to a total area of unity and includes all clusters identified by single linkage cluster analysis with a maximum HA nearest neighbor distance of 30 nm. Note the dramatic range (more than 50-fold) in cluster areas. Gaps in the line indicate zeros in the histogram.

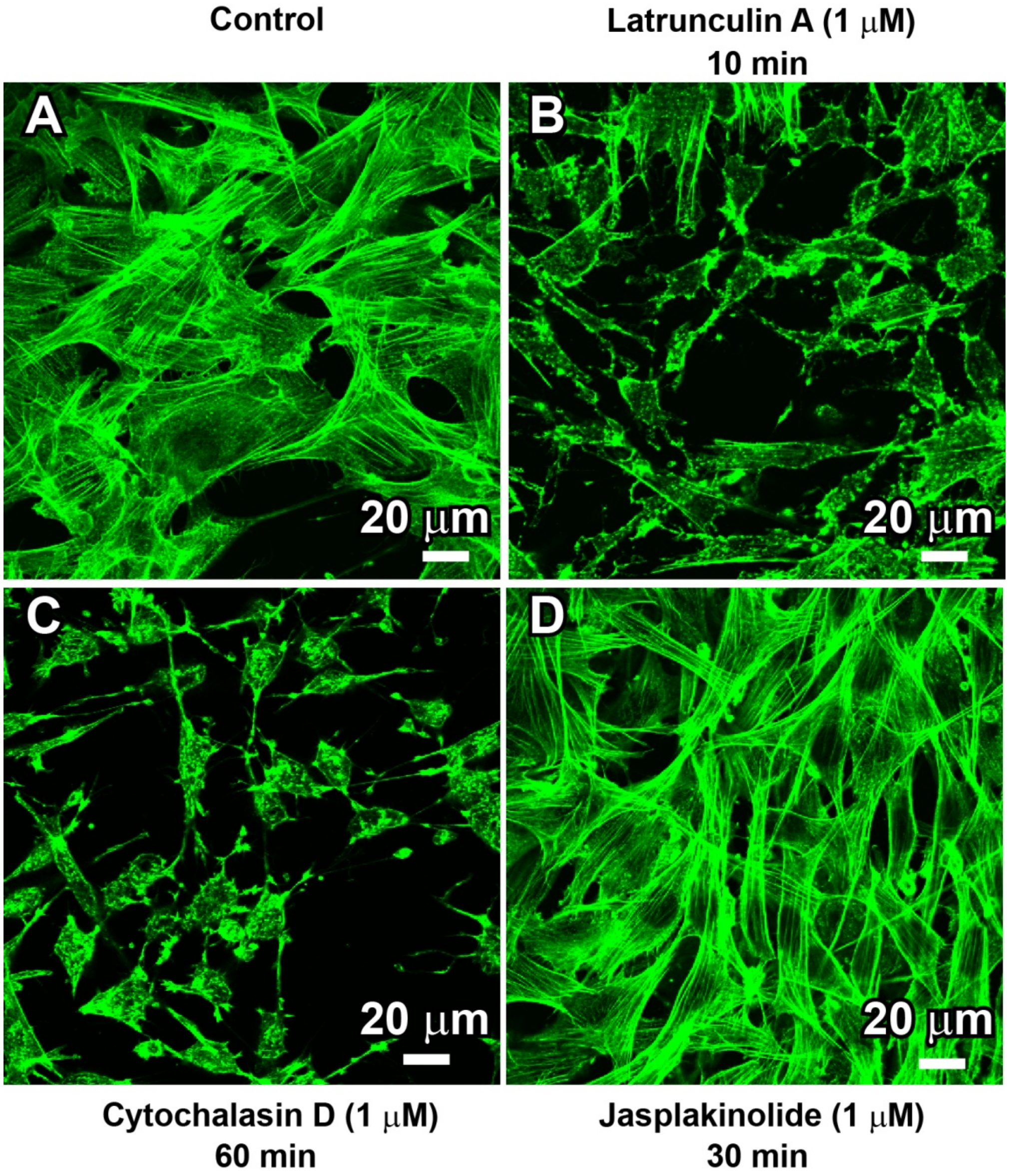

Figure S4. Actin disrupting drugs differentially affect actin structures in NIH3T3-HAb2 cells imaged by confocal microscopy. NIH3T3-HAb2 cells were incubated with actin disrupting drugs, fixed, stained with Alexa 488 phalloidin, and imaged by confocal microscopy. Actin disruption: (A) 0.01 % DMSO (vehicle control for actin disrupting drugs) for 60 min, (B) 1 μM latrunculin A (LatA) for 10 min, (C) 1 μM cytochalasin D (CytoD) for 60 min, and (D) 1 μM jasplakinolide (Jas) for 30 min. Note the substantial disruption of actin and cell rounding caused by LatA and CytoD. Jas-treated cells contained prominent and numerous intact actin stress fibers and showed very little cell rounding. Scale bar = 20μm.

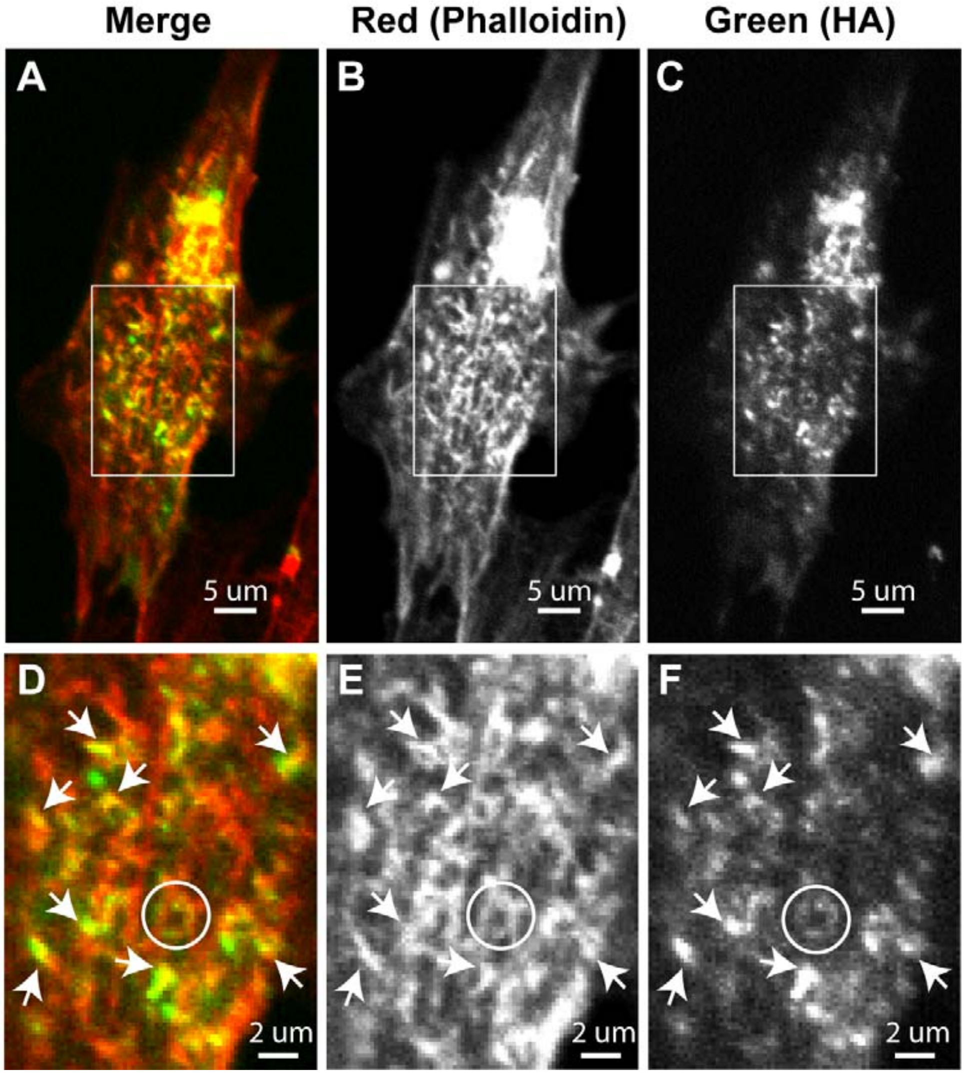

Figure S5. Confocal imaging of Dendra2-HA (green channel) and Alexa-680-phalloidin (red channel). NIH3T3-HAb2 cells transfected with Dendra2-HA were fixed, stained with Alexa-680-phalloidin then imaged on an Olympus FV-1000 confocal microscope with a 63x 1.42 NA objective and excitation at 488 nm and 635 nm. Shown is a projection of a 1.2 μm thick stack of ten slices at the bottom of the cell. Brightness and contrast were adjusted linearly for presentation. Note that Dendra2-HA and Alexa-680-phalloidin colocalize in some regions marked with white arrows and white circles. (A-C) Low magnification views of a single cell. (D-F) Zoomed region showed in white box in A-C. Scale bars 5 μm for A-C and 2 μm for D-F.

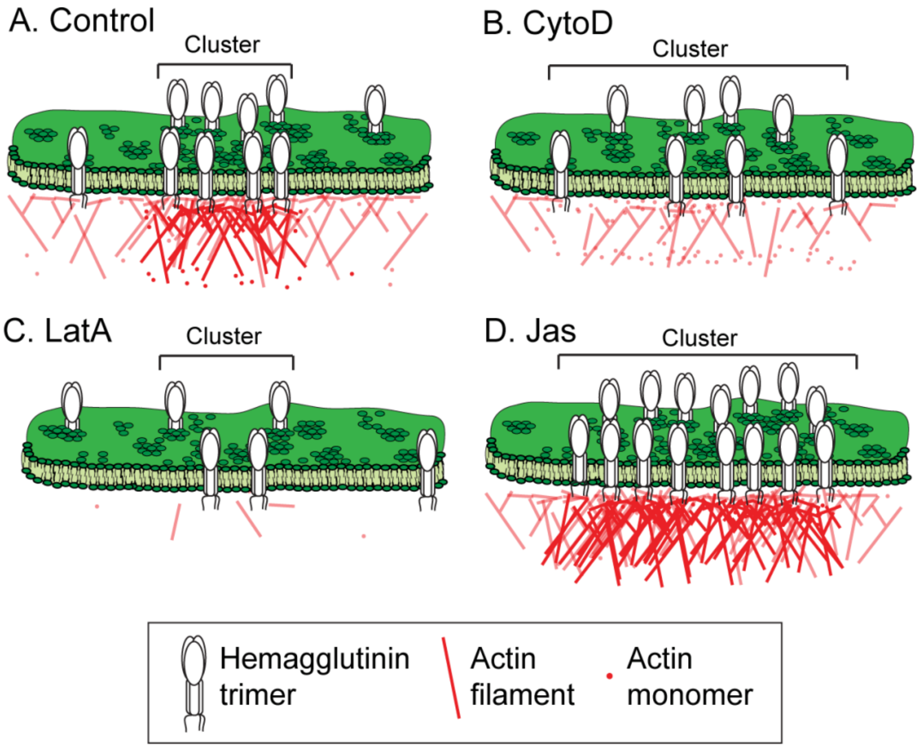

Figure S6. ***Actin disruption*****.** Models of LatA, CytoD and Jas treatments on HA cluster areas and densities in NIH3T3-HAb2 cells. (A) All effects are described with reference to the control (untreated, "Control") HA and actin distributions.

(B) Treatment with CytoD induces a lateral dispersion of clustered HA proteins. We propose that the loss of the underlying actin filaments and so loss of the structure maintaining the HA cluster disperses, allowing HA proteins to move laterally from the original cluster; and the average HA-HA nearest neighbor distance increases. However, intermolecular distances are still small enough for many of these proteins to be defined as within the same cluster and so the area of the clusters increases dramatically, but as the total number of molecules per cluster does not change, the cluster density reduces ("CytoD").

(C) Treatment with LatA caused a significant decrease in cluster density, and no change in cluster area. LatA could be expected to cause a more stringent assault than CytoD, as CytoD does not inhibit the nucleation of actin filaments *de novo*. After treatment, some proteins still retain nearest neighbor distances small enough to define them as being in a cluster. Unlike the CytoD treatment, intermolecular distances of many of these proteins now exceed that required to be defined as within the cluster. The number of proteins per cluster has reduced, the density has reduced, and the area covered by these now dispersed proteins has not changed ("LatA").

(D) Treatment with Jas inhibits depolymerization, so resulting in larger total amounts of filamentous actin. Before treatment, actin and HA clusters colocalized (e.g. Fig. 1). Jas treatment stabilizes and elongates filaments throughout the cell; as a greater concentration of these are adjacent to HA clusters the periphery of these actin meshworks is stabilized, and the structural basis for the cluster advances laterally. HA proteins which were non-cluster now associate, and cluster area increases, although cluster density remains unchanged ("Jas").

SUPPORTING REFERENCES

1. Gould, T. J., M. S. Gunewardene, M. V. Gudheti, V. V. Verkhusha, S. R. Yin, J. A. Gosse, and S. T. Hess. 2008. Nanoscale imaging of molecular positions and anisotropies. *Nature Methods* 5:1027-1030.
2. Subach, F. V., G. H. Patterson, S. Manley, J. M. Gillette, J. Lippincott-Schwartz, and V. V. Verkhusha. 2009. Photoactivatable mCherry for high-resolution two-color fluorescence microscopy. *Nature Methods* 6:153-159.
3. Gould, T. J., V. V. Verkhusha, and S. T. Hess. 2009. Imaging biological structures with fluorescence photoactivation localization microscopy. *Nature Protocols* 4:291-308.
4. Hess, S. T., T. P. K. Girirajan, and M. D. Mason. 2006. Ultra-high resolution imaging by fluorescence photoactivation localization microscopy. *Biophysical Journal* 91:4258-4272.
5. Hess, S. T., T. J. Gould, M. V. Gudheti, S. A. Maas, K. D. Mills, and J. Zimmerberg. 2007. Dynamic clustered distribution of hemagglutinin resolved at 40 nm in living cell membranes discriminates between raft theories. *Proceedings of the National Academy of Sciences of the United States of America* 104:17370-17375.
6. Thompson, R. E., D. R. Larson, and W. W. Webb. 2002. Precise nanometer localization analysis for individual fluorescent probes. *Biophysical Journal* 82:2775-2783.
7. Harris, A., G. Cardone, D. C. Winkler, J. B. Heymann, M. Brecher, J. M. White, and A. C. Steven. 2006. Influenza virus pleiomorphy characterized by cryoelectron tomography. *Proceedings of the National Academy of Sciences of the United States of America* 103:19123-19127.
8. Hess, S. T., M. Kumar, A. Verma, J. Farrington, A. Kenworthy, and J. Zimmerberg. 2005. Quantitative electron microscopy and fluorescence spectroscopy of the membrane distribution of influenza hemagglutinin. *Journal of Cell Biology* 169:965-976.
9. Schutz, G. J., H. Schindler, and T. Schmidt. 1997. Single-molecule microscopy on model membranes reveals anomalous diffusion. *Biophysical Journal* 73:1073-1080.
10. Semrau, S., and T. Schmidt. 2007. Particle image correlation spectroscopy (PICS): Retrieving nanometer-scale correlations from high-density single-molecule position data. *Biophysical Journal* 92:613-621.
11. Kusumi, A., Y. Sako, and M. Yamamoto. 1993. Confined lateral diffusion of membrane-receptors as studied by single-particle tracking (Nanovid Microscopy) - effects of calcium-induced differentiation in cultured epithelial-cells. *Biophysical Journal* 65:2021-2040.
12. Gunewardene, M. S., F. V. Subach, T. J. Gould, G. P. Penoncello, M. V. Gudheti, V. V. Verkhusha, and S. T. Hess. 2011. Super-resolution imaging of multiple fluorescent proteins with highly overlapping emission spectra in living cells. *Biophysical Journal* 101:1522-1528.
13. Bossi, M., J. Folling, V. N. Belov, V. P. Boyarskiy, R. Medda, A. Egner, C. Eggeling, A. Schonle, and S. W. Hell. 2008. Multicolor far-field fluorescence nanoscopy through isolated detection of distinct molecular species. *Nano Letters* 8:2463-2468.
14. Juette, M. F., T. J. Gould, M. D. Lessard, M. J. Mlodzianoski, B. S. Nagpure, B. T. Bennett, S. T. Hess, and J. Bewersdorf. 2008. Three-dimensional sub-100 nm resolution fluorescence microscopy of thick samples. *Nature Methods* 5:527-529.
15. Yeomans, J. M. 2002. Statistical mechanics of phase transitions. Oxford University Press, Oxford